Three-Dimensional, High Resolution, Computerized Ionospheric Tomographic Imaging and Computational Modeling of an Artificial Ionospheric Cavity

Craig A. Selcher

Dissertation submitted to the Eberly College of Arts and Sciences at West Virginia University in partial fulfillment of the requirements for the degree of Doctor of Philosophy in Physics

Mark Koepke, Ph.D., Chair

Earl Scime, Ph.D.

Art Weldon, Ph.D.

Boyd Edwards, Ph.D.

Paul Bernhardt, Ph.D.

Department of Physics

Morgantown, West Virginia

2007

UMI Number: 3300883

UMI®

Abstract

Three-Dimensional, High Resolution, Computerized Ionospheric Tomographic

Imaging and Computational Modeling of an Artificial Ionospheric Cavity

Craig A. Selcher

Tomographic techniques use line integral measurements to reconstruct local values of the measured parameter. These techniques have been applied to the ionosphere by using radio transmissions to measure the integral of electron density between a satellite and a chain of ground-based receiving stations. The resultant reconstructions form a two-dimensional map of the electron density in the plane of the satellite / receiver chain. Insufficient quantity of receivers and not having a complete range of accessible look angles with the available receivers are responsible for the non-uniqueness in the reconstructions. The limited look angle problem can be alleviated by making use of alternative data sources such as incoherent scatter radars (**ISR**) that provide information on the vertical structure of the electron density. The non-optimal receiver placement problem can be alleviated through the use of sophisticated reconstruction algorithms. The computerized ionospheric tomography (**CIT**) technique has recently been used to image the artificially modified ionosphere above the Arecibo Observatory (**AO**) HF heating facility. A total of nine radio beacon receivers forming a three by three matrix were deployed across the entire island of Puerto Rico. The arrangement maximizes the likelihood that several of the receiver-to-satellite lines of sight would intersect the heated region of the ionosphere. Several satellite passes associated with such an intersection occurred, and the resultant tomographic inversions

indicate the existence of an electron density cavity approximately 45 kilometers in latitudinal extent. The reduction of electron density in this cavity was typically on the order of 20%. The experimental observations were supported by theoretical work using the open-source SAMI2 ionospheric model. Methods were developed to model both the ohmic heating of the electrons and the suprathermal heating caused by nonlinear effects. Modeled ohmic heating values of 941 K/s match the observed heated temperature profiles. Modeled suprathermal electrons effects on the vibrational temperature of N_2 indicate a vibrational / translation temperature differential of 308° K.

DEDICATION

The author wishes to dedicate this work to his wife Trish, for her support,

encouragement and patience throughout this long process.

Table of Contents

Figure List

B. Introduction

B.1. What is Tomography?

The computerized ionospheric tomography (**CIT**) technique involves the transmission of a beacon radio signal through the ionosphere, typically from a satellite to a ground-based receiving system. The phase delay introduced into the signal by passage through the complex dielectric plasma medium of the ionosphere is extracted and used to determine the total electron count (**TEC**) between the transmitting and receiving locations. This TEC value and the ray-path geometry associated with each value are then incorporated into a reconstruction algorithm which forms two-dimensional maps of electron density. [1, 2]

The implementation of the ionospheric tomographic technique has traditionally been applied exclusively to naturally occurring, large-scale ionospheric structures. [3, 4, 5,]

---

[1] Bernhardt, P.A., R.P. McCoy, K.F. Dymond, J.Ml Picone, R. R. Meier, F. Kamalabadi, D.M. Cotton, S. Chakrabarti, T.A. Cook, J.S. Vickers, A.W.Stephan, L. Kersely, S.E. Pryse, I.K. Walker, C.N Mitchell, P.R. Straus, H. Na, C. Biswas, G.S. Bust, G.R. Kronschnabl, T.D. Raymund., Two-dimensional mapping of the plasma density in the upper atmosphere with computerized ionospheric tomography (CIT), *Phys. Plas., 5*, 2010-2021, May 1998.

[2] Austen, J.R., S.J. Franke, and C.H. Liu, Ionospheric imaging using computerized tomography, *Radio Science, 23*, 299-307, 1988.

[3] Kersley, l., Heatyon, J.A.T., S.E. Pryse, and T.D. Raymund, Experimental ionospheric tomography with ionosonde input and EISCAT verification, *Anns. Geophys., 11*, 1064-1074, 1993.

[4] Pryse, S.E., and L. Kersley, A preliminary experimental test of ionospheric tomography, *J. Atmos. Terr. Phys. 54*, 1007-1912, 1992.

[5] Pryse, S.E., L. Kersley, D.L. Rice, C.D. Russell, and I.K. Walker, Tomographic imaging of the ionospheric mid-latitude trough, *Anns. Geophys., 11*, 144-149, 1993.

[6, 7, 8, 9, 10, 11, 12] The work discussed here makes use of the small-scale spatial resolution available via the employment of relatively high data rate tomographic receiver systems. These systems record differential phase between two radio beacon signals at a rate sufficient to resolve any TEC structure of interest [13] to a degree comparable to one kilometer.

B.2. Experiment description

During the January 1998 Arecibo Observatory high power HF ionospheric heating campaign, an array of CIT receivers was deployed on the island of Puerto Rico, forming a dense, high resolution, three by three matrix. This arrangement allows, for the first time, three parallel reconstruction planes, each oriented approximately along a line of longitude, which are suitable for investigating changes in cavity extent both along and across the magnetic field lines. Measurements of TEC using the differential

---

[6] Raymund, T.D., J.R. Austen, S.J. Franks, C.H. Liu, J.A. Klobuchar, and J. Stalker, Application of computerized tomography to the investigation of ionospheric structures, *Radio Science*, *25*, 771-789, 1990.

[7] Raymund, T.D., Y. Bresler, D.N. Anderson, and R.E. Daniell, Model-assisted ionospheric tomography: A new algorithm, *Radio Science*, *29*, 1493-1512, 1994.

[8] Pryse, S.E., L. Kersley, M.J. Williams, and I.K. Walker, The spatial structure of the dayside ionosheric trough, *Ann. Geophysicae, 16*, 1169-1179, 1998

[9] Cook, J.A., S. Close, An investigation of TID evolution observed in MACE '93 data, *Ann. Geophysicae, 13*, 1320-1324, 1995

[10] Pryse, S.E. C.N. Mitchell, J.A.T. Heaton, L. Kersley, Travelling ionospheric disturbances imaged by tomographic techniques, *Ann. Geophysicae, 13*, 1325-1330, 1995

[11] Bust, G.S.; Gaussiran, T.L., II; Coco, D.S., Ionospheric observations of the November 1993 storm, *J. Geophys. Res.*, *102*, 14293-14304, 1997

[12] Kronschnabl, G.R.; Bust, G.S.; Cook, J.A.; Vasicek, C.J., Mid-America computerized ionospheric tomography experiment (MACE '93), *Radio Science, 30*, 105-108, 1995

[13] Leitinger, R., Data from orbiting navigation satellites for tomographic reconstructions, *Int. J. Imaging Syst. Technol., 5*, 86-96, 1994

Doppler technique were made during both heater-on and heater-off periods. To supplement this closely spaced data set, the Applied Research Lab (**ARL**) of the University of Texas at Austin made available the data from a chain of CIT receivers deployed throughout the Caribbean region. Vertical profiles of electron density were obtained by use of the Incoherent Scatter Radar (**ISR**) at the Arecibo Observatory, and were used both to determine the absolute value of TEC and to form empirical initial conditions for the reconstructions.

B.3. Data discussion and Summary

Reconstructions generated using code developed at the Naval Research Laboratory (**NRL**) by the author (see Appendix A) clearly indicate the existence of electron density cavities consistent with previous measurements [14, 15, 16] and demonstrate the applicability of CIT to the imaging of artificial structures formed in an high-frequency (**HF**) heated ionosphere. In addition, since the differential phase technique solely measures the electron density, CIT may be of assistance in resolving the electron density / temperature ambiguity present in ISR measurements.[17] We considered limitations to the CIT results and found that by using closely-spaced 3-receiver chains we can resolve and investigate artificially generated structures which are

---

[14] Hansen, J.D., Morales, G.J., Duncan, L.M., Dimonte, G., Large-scale HF-induced ionospheric modifications: Experiments, *JGR, 97*, 113-122, 1992

[15] Bernhardt, P. A., C. A. Tepley, and L. M. Duncan, Airglow enhancements associated with plasma cavities formed during ionospheric heating experiments, *J. Geophys. Res., 94*, 9071-9092, 1989.

[16] Duncan, L.M., J.P. Sheerin, R.A. Behnke, Observations of ionospheric cavities generated by high-power radio waves, *Phys. Rev. Lett., 61*, 239-242, 1988

[17] Sulzer, M.P., A radar technique for high range resolution incoherent scatter autocorrelation function measurements utilizing the full average power of klystron radars, Radio Sci., 21, 1033, 1986

of a much smaller dimension than the naturally occurring ionospheric structures which had been previously imaged using the CIT technique.

C. Context of the problem: The Earth's ionosphere.

C.1. Defined and described

The Earth's ionosphere is typically taken to be that region of the upper atmosphere where plasma is present and has sufficient density to affect the propagation of electromagnetic waves, particularly those in the radio frequency range. This region begins near 80 km in altitude and extends to and merges with the magnetosphere at roughly 1000 km altitude. The upper and lower boundaries of the ionosphere are not well-defined, and shift according to diurnal and seasonal variations and other processes. By convention, the ionosphere is divided into a number of layers, denoted by the letters D, E, and F. The D-region extends from roughly 50 to 90 km, the E-region extends from 90 to 150 km, and the F-region comprises the remaining portion of the ionosphere from 150 km to 1000 km Once again, these boundaries are not well-defined, and vary as ionospheric conditions change. [18]

The D region is very weakly ionized, highly collisional, and primarily composed of molecular oxygen ions (O_2^+) and nitric oxide ions (NO^+). For the purposes of this study, the sole effect of the D region is to absorb a negligibly small portion of the beacon radio signal. Assuming that the beacon frequency is much greater than the electron-neutral collision frequency, and neglected effects due to the geomagnetic field, the absorption coefficient is,

$$\kappa = 1.15 x 10^{-3} \frac{N\nu}{f^2}$$

---

[18] Rishbeth, H., O.K. Garriot, Introduction to Ionospheric Physics, New York: Academic Press, 1969

in units of decibels per kilometer, and where N is the electron density, ν is the electron-neutral collision frequency, and f is the beacon frequency. Typical D-region values of ν (10^8/s) and N (10^3 electrons/cm^3) result in $\kappa = 5.1 \times 10^{-8}$. The total attenuation through the D-region is therefore approximately 1.53×10^{-7} dB, and is clearly negligible.

The E region, extending from 90 km to 150 km, is also composed primarily of molecular oxygen ions (O_2^+) and nitric oxide ions (NO^+). Typical E region peak electron concentrations are on the order of 10^5 electrons/cm^3. The time constants associated with the various chemical processes that occur at E region heights are short enough that transport can be neglected, and photochemistry dominates.

The F-region, extending from 150 km to 1000 km, is predominantly populated with oxygen ions (O^+). At the uppermost portion of the ionosphere near 1000 km altitude, helium ions (He^+) and hydrogen ions (H^+) are the dominant species.[19] Typical F region peak densities are on the order of 10^6 electrons/cm^3. The F region is frequently conceptually divided into three sub-regions based upon the predominant physical processes in each sub-region. The lowest region is dominated by photochemistry, has negligible diffusion, and is known as the F1 region. The region near the peak electron concentration profile corresponds to a transition from photochemical dominance to diffusion dominance, and is called the F2 region. The upper F region , dominated by diffusion, is called the topside of the ionosphere. It is clear that due to both its spatial extent and high concentration, the bulk of the ionospheric plasma lies in the F-region.

---

[19] Kelley, M.C., The Earth's ionosphere, Academic Press, 1989

Since the total electron content (TEC) is a measure of the integrated electron density, the most significant contribution to the measured TEC is from the F-region.

The primary production mechanism for both the F and E regions is photo ionization by the absorption of solar photons by the neutral atmospheric gas. A useful analytic model which serves to quantitatively describe the core features of this mechanism is known as the Chapman model, and is described in detail in section C.3. The steady-state ionospheric electron concentration profile is determined by the combination of production, primarily the photo ionization described in section C.3, and loss through recombination and transport, and is described in section C.4. The resultant mathematical model of the ionosphere, which combines the primary qualitative features of these mechanisms and captures the major characteristics of a quiet mid-latitude ionosphere, is described in section C.5.

C.2. The mid-latitude ionosphere at Arecibo

The ionosphere at the latitude of the Arecibo Observatory exemplifies the mid-latitude ionosphere. The geomagnetic dip angle (the angle at which the Earth's magnetic field passes through the ionosphere) is 50° with respect the horizontal. This allows for some degree of freedom for the upward and downward flow of charged particles, since that flow is constrained to be parallel or antiparallel to the magnetic field. The geomagnetic latitude is 34°, which is far from both the auroral oval at 70° geomagnetic latitude and the energetic precipitating particles to be found there. Consequently, the mid-latitude ionosphere is relatively "quiet" compared to the

tumultuous auroral (or near auroral) ionosphere at the latitude of many of the other
ionospheric research facilities. [20]

C.3. Chapman Production Function Theory

The analytic approach used in this work to provide a theoretical description of
the generation mechanism of the ionosphere is known as Chapman theory. Several
simplifying assumptions are made to make the problem tractable. The first assumption
is that the sole source of ionization is photo ionization by absorption of solar radiation.
This radiation is modeled as having a single value for the absorption cross section, and
the absorbing atmospheric gas is assumed to be composed of a single constituent which
is planar, horizontally stratified, and in hydrostatic equilibrium.[21]

Hydrostatic equilibrium results in a vertical profile of neutral gas density which
obeys:

$$n_n(h) = n_o \exp\left(-\frac{(h - h_o)}{H_n}\right)$$
(C.3.1)

where n_o is the neutral density at reference height h_o and $H_n = kT_n/m_n g$ is the exponential
scale height of the neutral gas. This exponential decrease in neutral density with height
is a result of balancing the effect of gravity on the gas with the thermal pressure within
the gas.

Chapman theory avoids dealing directly with the complex nature of the radiative
transfer of energy through the neutral gas by folding all photon absorption details into

[20] Sojka, J.J., Ionospheric physics, *Rev. of Geophys., Supp.,* 1166-1186, 1991

[21] Chapman, S., The theoretical height distribution of band-absorbed solar radiation, *Proc Phys Soc (London), 51,* 93-109

the photon absorption cross section σ and using an ionization probability η to convert

the energy absorbed into the number of electrons released from the neutral gas. The

rate of electron production q can therefore be given by

$$q = \eta \sigma n_n I ,$$ (C.3.2)

where η is the ionizing efficiency (photoelectrons produced per photon absorbed), σ is

the cross section of absorption, n_n is the neutral gas density, and I is the radiation

intensity.

The geometry of this situation is shown in Figure 1a. As the radiation is

absorbed, its intensity will fall off with distance along the line of sight s,

$$-\frac{dI}{ds} = \sigma n_n I ,$$ (C.3.3)

as can be seen in Figure 1b. Note that the electron production is proportional to the rate

at which radiation is absorbed, i.e., $q = -\eta \dfrac{dI}{ds}$

The electron production rate q reaches a maximum when, according to C.3.2

$$\frac{dq}{ds} = \eta \sigma \left(I \frac{dn_n}{ds} + n_n \frac{dI}{ds} \right) = 0$$ (C.3.4)

Combining the trigonometric relation between line-of-sight path length s and

height $h, \dfrac{dh}{ds} = -\cos(\chi)$, and the hydrostatic expression for n_n (C.3.1), yields,

$$\frac{1}{n_n} \frac{dn_n}{ds} = \frac{\cos(\chi)}{H_n} ,$$ (C.3.5)

Substitution of C.3.5 in C.3.4 shows that for the location of maximum

photoelectron production,

$$\sigma H_n n_m \sec(\chi) = 1,$$ (C.3.6)

where the subscript m indicates the neutral density measured at the maximum of electron production. This can be written in simplified form as $\sigma N_{nm} = 1$, where

$$N_{nm} = \int_{\infty}^{s_m} n \, ds$$ is the integrated neutral density from infinity to the location of the production maximum at s_m.

Integrating C.3.3 to obtain I as a function of s, and extending our use of N_{ns} to indicate the neutral density integral, we have,

$$\frac{dI}{I} = d(\ln I) = -\sigma n_n ds,$$

$$\ln\left(\frac{I(s)}{I_\infty}\right) = -\sigma \int_{\infty}^{s} n_n ds = -\sigma N_{ns},$$

$$I(s) = I_\infty \exp(-\sigma N_{ns}).$$ (C.3.7)

Combining C.3.2, C.3.6 and C.3.7 leads to a peak production rate of

$$q_m = \eta \sigma n_m I_m = \eta \sigma \frac{I_\infty \exp(-1)}{\sigma H_n \sec(\chi)} = \frac{\eta I_\infty \cos(\chi)}{H_n \exp(1)},$$ (C.3.8)

since $\sigma N_{nm} = 1$ at the production peak. The height at which this maximum occurs can be determined by inserting the hydrostatic equation into (C.3.6),

$$\sigma H_n n_o \exp\left(-\frac{(h_m - h_o)}{H_n}\right)\sec(\chi) = 1,$$

and solving for h_m,

$$h_m = h_o - H_n \ln\left(\frac{\cos(\chi)}{\sigma H_n n_o}\right).$$ (C.3.9)

From C.3.7 and once again using the relationship between s and h, we can

determine $I(h)$,

$$I(h) = I_\infty \exp\left[-\sigma n_o H_n \sec(\chi) \exp\left(-\frac{(h - h_o)}{H_n} \right) \right],$$ (C.3.10)

and subsequently the production rate q as a function of height,

$$q(h) = \eta \sigma n_n I = \eta \sigma n_o I_\infty \exp\left[-\frac{(h - h_o)}{H_n} - n_o \sigma H_n \sec(\chi) \exp\left(-\frac{(h - h_o)}{H_n} \right) \right].$$ (C.3.11)

From C.3.8, $\eta I_\infty = q_m \dfrac{\exp(1) H_n}{\cos(\chi)}$, and using the value of h_m from C.3.9,

$$q = q_m \exp\left[1 + \frac{(h_m - h)}{H_n} - \exp\left(\frac{(h_m - h)}{H_n} \right) \right].$$ (C.3.12)

Substituting $z = \dfrac{(h - h_m)}{H_n}$ results in the simple expression for the Chapman

production function q,

$$q = q_m \exp[1 - z - \exp(-z)].$$ (C.3.13)

A representative example of the Chapman production function is shown in

Figure 2. One of the primary variations of the actual photoionization profiles from the

simplest Chapman theory is due to the multi-component nature of the neutral

atmospheric gas and the wavelength dependent absorption coefficient of the incoming

solar radiation. These two factors lead to complexity in the absorption and production

profile compared to the simple profile depicted in Figure 2.

A portion of this complexity can be accounted for by separating the absorption

components into three bands. Figure 3a is a plot of the height at which incoming solar

radiation will be reduced to 1/e of its original intensity, as a function of the wavelength of the incoming radiation. From equation C.3.7, it can be seen that this corresponds to the height of the production maximum. Wavelengths below 20 nm and above 80 nm are primarily responsible for the production of the E region. The wavelength band between 20 nm and 80 nm is primarily responsible for the production of the F region. Figure 3b shows the Chapman photoionization production rates for each of these bands as functions of height. The long-term structure of the ionosphere is to a large degree a combination of the photoionization production described in this section and the loss and transport mechanisms described in section C.4

C.4. Loss, Transport, and the Equilibrium Ionosphere

There are several recombination process which are responsible for the bulk of the loss of oxygen ions, the predominant ion in the F region. These process are given by:

$$O + hv \rightarrow O^+ + e \hspace{4cm} \text{C.4.1}$$

$$O^+ + N_2 \rightarrow NO^+ + N \hspace{4cm} \text{C.4.2}$$

$$NO^+ + e \rightarrow N + O \hspace{4cm} \text{C.4.3}$$

$$O^+ + O_2 \rightarrow O_2^+ + O \hspace{4cm} \text{C.4.4}$$

$$O_2^+ + e \rightarrow O + O \hspace{4cm} \text{C.4.5}$$

Equation C.4.1 represents direct radiative recombination, and occurs slowly enough to be ignored. Equations pairs C.4.2, C.4.3 and C.4.4, C.4.5 are ion-atom interchange reactions followed by dissociative recombination of the resultant molecular ion. These two reaction pairs are the primary recombination mechanisms for the oxygen ions in the F region.

For the regions where photochemistry dominates, the E and F1 regions, transport is ignored and the continuity equation for species j becomes

$$\frac{dn_j}{dt} = P_j - L_j \hspace{4cm} \text{C.4.6}$$

where P_j is the production rate and L_j is the loss rate. For steady-state conditions, $\frac{dn_j}{dt} = 0$, hence $P_j = L_j$ and the loss rate due to recombination is proportional to the product of the densities of the two recombining species. If it is assumed that one ion

species dominates (which is reasonably valid for oxygen ions in the F1 and F2 regions), then the density of that ion is equal to the electron density, and the recombination loss term can be expressed as $P_j = L_j = \alpha n_e^2$, where α is the ion-electron recombination rate. Using the Chapman production function C.3.13, we have

$$\alpha n_e^2 = q_m \exp[1 - z - \exp(-z)]$$

$$n_e = \left(\frac{q_m}{\alpha}\right)^{\frac{1}{2}} \exp\left\{\frac{1}{2}[1 - z - \exp(-z)]\right\}. \qquad \text{C.4.7}$$

In the E region, the recombination-rate coefficient α is relatively independent of altitude and concentrations of minor constituents, and the electron density profile can be expected to follow Equation C.4.7 in a relatively uncomplicated manner. At F1 region heights, where photochemistry still dominates the physics and diffusion is not a significant factor, but the recombination-rate coefficient is not independent of altitude and concentrations of minor constituents, the result is more complicated.

An expression which illustrates this more complicated behavior can be derived by again assuming a steady state and equating the production function C.3.13 for oxygen ions with the loss terms for those ions shown in equations C.4.2 – C.4.5:

$$n_{O+} = \frac{q_{O+}}{\alpha_{N2} n(N_2) + \alpha_{O2} n(O_2)}, \qquad \text{C.4.8}$$

where α_{N2} and α_{O2} are the chemical rate constants associated with the ion-atom interchange/dissociative recombination reactions from equations C.4.2 – C.4.5, and $n(N_2)$ and $n(O_2)$ are the densities of the molecular nitrogen and oxygen respectively.

The numerator in equation C.4.8 is the production function C.3.13 for oxygen ions, and decreases exponentially with altitude since it is directly proportional to the exponentially decreasing atomic oxygen density (recall from figures 3a and 3b that the peak of the production function is at around 150 km). However, the recombination rates α_{N2} and α_{O2} are directly proportional to the molecular oxygen (O_2) and nitrogen (N_2) densities, which fall off at an even greater exponential rate due to their greater molecular weight. This leads to a resultant exponential increase in oxygen ion concentration with height throughout the F1 region until diffusion begins to play a role at F2 region heights.

In the topside ionosphere, above the F2 region, diffusion dominates photochemistry, and the ion concentration follows a diffusive equilibrium profile. The classical diffusive equilibrium equation is given by

$$\frac{1}{n_j}\frac{\partial n_j}{\partial r} = -\frac{1}{H_j} - \frac{1}{T_j}\frac{\partial T_j}{dr} \qquad\qquad C.4.9$$

where n_j is the density of species j, T_j is the temperature of species j, and

$$H_j = \frac{2kT_j}{m_j g} \qquad\qquad C.4.10$$

is the scale height for species j. C.4.9 is easily solved with the assumption of an isothermal ionosphere, $\dfrac{\partial T_j}{dr} = 0$, and the result is

$$n_j = n_{j0}\exp\left[-\frac{(r-r_0)}{H_j}\right] \qquad\qquad C.4.11$$

This results in a density profile which exponentially decreases with height in the diffusion dominated topside region. Figure 4 illustrates the competing processes which contribute to the equilibrium density profile of the ionospheric F region.

C.5. The Five-Parameter "Chapman" Model

The characteristics of the multiply exponential profile described in section C.4 are reasonably well represented by modifying the Chapman production function by both increasing the scale height and the peak altitude to account for the variation from a direct photochemical profile. The scale height then represents an effective scale height which includes diffusive effects, and the peak height provides indication of the crossover point between photochemistry and diffusion dominance. Other modification can be made to the simple Chapman function to account for the multiple species present in the ionosphere. The five-parameter Chapman model used in this work includes both a small linear and a quadratic variation of the scale height H_n with altitude above the density peak. This results in a more accurate description of the topside of the ionosphere where the primary constituents are hydrogen and helium rather than oxygen, since their smaller molecular weight results in a more gradual density decrease compared to oxygen. This five-parameter model is given by:

$$n = n_{max} \exp\left[1 + \frac{(h_{max} - h)}{H_0} - \exp\left(\frac{(h_{max} - h)}{H_0}\right)\right]; \qquad h < h_{max}$$

$$n = n_{\max} \exp\left[1 + \frac{\left(h_{\max} - h\right)}{H_0 + H_1\left(h_{\max} - h\right) + H_2\left(h_{\max} - h\right)^2} - \exp\left(\frac{\left(h_{\max} - h\right)}{H_0 + H_1\left(h_{\max} - h\right) + H_2\left(h_{\max} - h\right)^2}\right)\right]$$

; h >= h_{max}

where H_0 is the unadjusted scale height, H1 is the linear contribution to the effective

scale height and H_2 is the quadratic contribution to the effective scale height.

D. Experimental Method: Computerized Ionospheric Tomography

D.1. Total Electron Content

D.1.a. Differential phase

We arrive at a two-dimensional map of electron density in an altitude-latitude plane by measuring the differential phase between two beacon signals transmitted by a single satellite and received by an array of receivers. Differential phase is a technique which measures the line-integral of electron density by comparing the phases of two mutually coherent radio signals which are transmitted simultaneously but at two separate frequencies.[22, 23] For the Navy Navigation Satellite System (NNSS, or "Transit") satellites used in these experiments, the beacon frequencies are 150 MHz and 400 MHz (each -80 ppm).[24] Naturally, the relative phase increases as the two signals propagate, and so as the transmitter-receiver distance evolves, the measured phase varies in a predictable fashion.

If, however a dielectric medium with a frequency-dependent dielectric function exists along the path, then a relative phase shift is introduced between the two signals. This relative phase shift reflects the details of the electron density along the path, since for high frequency waves in plasmas, the ions are virtually static and the dielectric properties of the medium are characterized by the electron motion. The measured phase shift is an accumulation of the effects integrated along the line of sight.

[22] Garriot, O.K., A.V. DaRosa, W.J. Ross, Electron content obtained from Faraday rotation and phase path length variations, *Journal of Atmospheric and Terrestrial Physics, 32*, 705-727, 1970

[23] Leitinger, R., G.K. Hartmann, F.J. Lohmar, E. Putz, Electron content measurements with geodetic doppler receivers, *Radio Science, 19*, 789-797, 1984

[24] Newton, R.R., The Navy Navigation satellite system, *Space Res, 7*, 735-763, 1967

The phase accumulated by a radio wave as it passes through a dielectric medium is given by,[25]

$$\Phi = 2\pi \int \frac{ds}{\lambda} = \frac{2\pi}{\lambda_o} \int \mu ds \text{ , in radians,} \tag{D.1.1}$$

where λ is the wavelength, λ_o is the free space wavelength, and μ is the dielectric constant,

$$\mu^2 = 1 - \left(\frac{e^2}{4\pi^2 \varepsilon_o m_e} \right) \left(\frac{N}{f^2} \right) = 1 - 80.6 \left(\frac{N}{f^2} \right). \tag{D.1.2}$$

Assume N/f^2 is small, and by expansion,

$$\mu = 1 - 40.3 \left(\frac{N}{f^2} \right). \tag{D.1.3}$$

The measured phases for two beacon signal can then be described by,

$$\Phi_1 \lambda_1 = \int \mu_1 ds = \int ds - \frac{40.3}{f_1^2} \int N ds = S_1 - \frac{40.3}{q_1^2 f_o^2} N_T$$

$$\Phi_2 \lambda_2 = \int \mu_2 ds = \int ds - \frac{40.3}{f_2^2} \int N ds = S_2 - \frac{40.3}{q_2^2 f_o^2} N_T \tag{D.1.4a, b}$$

where λ is the free space wavelength for the beacon signal, q is the ratio of the frequency of the beacon signal to the reference frequency f_o, S is the free space path length for the beacon signal, and N_T is the integrated electron density along the beacon signal path. Assuming that refractive effects are negligible leads to $S_1 = S_2$, and using the relation $\lambda_1 = f_1 c = q_1 f_o c$, the phase difference is given by

---

[25] Davies, K., Ionospheric Radio, London: Peter Peregrinus Ltd., 1990

$$\Delta\Phi = \frac{\Phi_2}{q_2} - \frac{\Phi_1}{q_1} = \frac{40.3N_T}{f_o c}\left(\frac{1}{q_1^2} - \frac{1}{q_2^2}\right), \text{ in cycles, and} \qquad (D.1.5)$$

$$\Delta\Phi = \frac{80.6\pi N_T}{f_o c}\left(\frac{1}{q_1^2} - \frac{1}{q_2^2}\right), \text{ in radians,} \qquad (D.1.6)$$

Solving for N_T, the Total Electron Content (TEC) yields

$$N_T = \frac{(f_o c \Delta\Phi)}{80.6\pi\left(\frac{1}{q_1^2} - \frac{1}{q_2^2}\right)}, \qquad (D.1.6)$$

and this can be expressed as

$$N_T = \alpha\Delta\Phi \ \text{ where } \alpha = \frac{f_o c}{80.6\pi\left(\frac{1}{q_1^2} - \frac{1}{q_2^2}\right)} \approx 6.21\times10^{14} \frac{\text{electrons}}{\text{m}^2 \cdot \text{radian}} \text{ for the Transit beacon,}$$

for which f_o=50 MHz, q_1=3 and q_2=8.

As an example, the differential phase that would be observed for the signals from the beacon onboard the Transit satellites (transmitting at 150 MHz and 400 MHz) after passing through one kilometer of plasma with a density of 10^5 electrons/cm^3 (a typical F-layer peak density) would be 0.161 radians.

D.1.b. Geophysical constraints and limitations

D.1.b.i. Phase ambiguity

The fact that $\Phi_o = m(2\pi) + \Phi_o$ is an ambiguity that introduces an uncertainty into the measured signal at both the beginning of measurement and at each reacquisition. Reacquisition occurs sometime after the phase lock loop between the receiver and the incoming radio wave is lost, which happens occasionally in the real-

world environment. Typically data is discarded when the phase lock is lost if the

satellite has traveled a significant distance during the loss (e.g. greater than 20 km or 2

sec). For short periods of phase lock loss, interpolated data may be generated and

substituted for the missing data.

D.1.b.ii. Offset uncertainty

Upon initial acquisition of the satellite at the horizon, there exists an uncertainty

in the value of the received phase, and consequently the absolute value of TEC. This

uncertainty amounts to an offset, the value of which is adjusted to match either a model-

based assumption that is made about the ionosphere or a direct empirical measurement

made by a supplemental diagnostic. [26, 27, 28] This uncertainty in initial phase means that

the measured TEC will be a relative value rather than an absolute value until the offset

is determined independently.

D.1.b.iii. Refractive effects

Refractive effects on the ray path of the beacon signal due to the undisturbed

background ionosphere are negligibly small, since the frequency of lowest component

of the beacon signal, at 150 MHz, is much greater than the maximum ionospheric

plasma frequency during these experiments of approximately 5 MHz. Assuming a

nominal, spherically symmetric, electron-density profile results in an angular deflection

---

[26] Austen, J. R., and S. Chalasani, Integrating ionosonde data into computerized ionospheric tomography, *Proceedings of the International Beacon Satellite Symposium, Abserwyth Wales*, July 1994.

[27] Heaton, J.A.T., S.E. Pryse, L. Kersley, Improved background representation, ionosonde input and independent verification in experimental ionospheric tomography, *Anns. Geophys*., *13*, 1297-1302, 1995.

[28] Page, D.L.; Austen, J.R., Comparison of tomographic and conventional methods for resolution of the constant of integration, *Radio Science, 32*, 1645-56, 1997

of the apparent direction of the signal from the true direction of the signal of less than

one-hundredth of a degree.   Thus refractive bending of the beacon signal due to the

natural ionosphere can be ignored.

The bending of the beacon signal ray path due to the horizontal gradients of

electron density along the edges of the large-scale artificially-generated cavity which is

the focus of this work, and is described in detail in section G, can be derived from

equation D.1.4. This effect is known as wedge refraction, and the bending angle which

results is expressed by

$$\delta = \frac{40.3}{f^2} \frac{\partial N_T}{\partial x} \qquad\qquad\qquad\qquad \text{D.1.7}$$

The maximum horizontal gradient in the TEC for this experiment (seen in Figure 16c) is

6.176×10^{10} m^{-2}m^{-1}, resulting in a bending angle δ of 1.1×10^{-4} radians for the 150 MHz

component of the beacon signal. The lateral deviation at the ground due to this bending

over the 1000 km propagation path is approximately 50 meters, far less than the

reconstruction pixel size and therefore having no significant impact.

D.2. Computerized Ionospheric Tomography explained

A single line-integral measurement of a structured medium is incapable of

resolving that structure. However, sufficient sampling over a complete range of angles

throughout the medium can be synthesized to form a reconstructed image of the

structure. Insufficient sampling introduces a non-uniqueness to the image and

contributes to the generation of numerical artifacts in the reconstructed image. In our

case, where all sampling of the ionosphere is from lines originating on the ground and

aimed upward, we have an ill-posed problem.[29] In the near future, satellite-to-satellite integration paths will make horizontal sampling possible, dramatically improve vertical resolution, and eliminate the non-uniqueness,[30, 31] but presently this capability is absent. Present options to minimize the non-uniqueness of the image involve either the use of alternate measurement techniques to augment the TEC measurements, the use of a model to restrict the structure geometry, or both. Both a TEC-derived Chapman model and supplementary measurements of the electron vertical profile data using the ISR at the Arecibo Observatory have been used in this work

D.3. Geometric Requirements

To reconstruct two-dimensional structure, the paths associated with the line averages should share the same plane and should intersect. Sampling the same plane from different perspectives not only gives the variation of TEC for each line but also specifies where along each line the variations occur. The sampling of the differential phase of the received beacon signal at discrete times selects specific ray paths used in the reconstruction process. The resolvability of the structure depends on the density of intersections and the range of angles of the ray paths in a given sub-region.[32] For the application of tomography to ground-based beacon receivers, the horizontal resolution

[29] Yeh, K.C. and T.D. Raymund, Limitations of ionospheric imaging by tomography, *Radio Science*, *26*, 1361-1380, 1991.

[30] Bernhardt, P.A., K.F. Dymond, J.M. Picone, D.M. Cotton, S. Chakrabarti, T.A. Cook, and J.S. Vickers, Improved radio tomography of the ionosphere using EUV/optical measurements from satellites, *Radio Science, 32*, 1965-1972, 1997

[31] Bernhardt, P.A., C.A. Selcher, S. Basu, G. Bust, S. Reising, Atmospheric Studies with the Tri-Band Beacon Instrument on the COSMIC Constellation, *TAO, 11,* 291-312, 2000

[32] Biswas, C., H. Na, Resolution and coverage analysis for ionospheric tomography, *Radio Science, 35*, 905-920, 2000

depends predominantly on the distance between neighboring receiver sites, whereas the

vertical resolution depends predominantly on the overall extent of the array. Since a

specific sub-region is reconstructed using ray paths from different receivers taken at

various times, the assumption of a steady state ionosphere, and its structure, is implied

for the duration of a given satellite pass. The reconstruction of a three dimensional

structure requires multiple linear arrays, each resolving a different plane.

Ideally, each array of receivers should be strictly one dimensional and parallel to

the ground track of each satellite pass. Due to variations within the ensemble of

satellite passes and due to geographical and political constraints in choices of receiver

sites, this ideal configuration is not achievable in real-world deployments. Violating

these assumptions results in site-to-site differences in receiver-satellite sight angles and

consequently the sampling plane of each receiver is not coplanar with the others in the

chain. Variance from this guideline is acceptable so long as the site-to-site deviation is

much less than the scale of the ionospheric structure under investigation. For this work,

the site-to-site variance was less than a few kilometers, and the scale size of the heated

volume being studied was on the order of fifty kilometers, satisfying the criteria for the

chain being sufficiently collinear.

D.4. Generalized observing scheme

Figure 5 shows a generalized array of 7 receiver sites and a family of sight lines

from each one. Notice that the region of maximum density of line intersections occurs

above the central receiver sites. Within this region, the intersection density has a

maximum at an altitude that depends on the distance between neighboring receiver

sites. The regions above the edge receivers suffer from both low intersection-point density and narrow angle range associated with the intersecting lines. The region beyond the last receiver site suffers so much from these effects that the image in that region is assigned a minimal accuracy.

D.5. Methodology

The reconstruction of the ionospheric structure in a given plane with this method takes place on a grid superposed onto the region of interest, which extends between the satellite path and the receiver array. This region is centered around the F layer at approximately 300 km, an altitude where the overwhelming percentage of plasma exists. Boundaries are chosen at 100 km and 600 km altitude to ensure that all pertinent TEC information is included. Boundaries on the north and south are set to be just outside of the northernmost and southernmost receiver sites, respectively.

The mesh size of the reconstruction grid is chosen to balance computational efficiency and the desire to resolve the details of the plasma structure in the ionosphere. A 5 km mesh size was chosen in order to clearly resolve the artificially generated cavity (expected to be on the order of 40 km), to take advantage of the high-density spatial deployment of the beacon receivers, and to fully utilize the 50 Hz data-sampling rate of the 1502 DS receivers. The confidence in the electron density value assigned to each mesh cell improves with each additional ray path having a distinctly different angle through the cell. For a given mesh cell, the number of intersecting ray paths representing distinctly different intersection angles is approximately the number of receiver sites in the array. Therefore the confidence can be limited either by the

available budget in receivers and their deployment or by the geographic extent of the receiver site array, or both. In the case reported here, the limitation was the small size of the island of Puerto Rico on which the Arecibo Observatory is located, and the lack of any other nearby islands to the north or south of Puerto Rico.

D.6. Algorithm

Tomographic techniques use line integral measurements to reconstruct local values of the measured parameter. This requires a large number of measurements to be taken for many paths and angles that pass through the object under study. In this case, the object under study is the ionosphere, and the parameter being measured is the electron density. A number of different tomographic methods exist, and a finite-series expansion method was chosen for this work due to its adaptability to a multitude of geometries and conditions.[33, 34, 35]

Let G(r,ϕ) be the local electron density in the satellite-receiver image plane, where r is the distance from the center of the Earth, and ϕ is the angle of latitude. If p_i is defined as the path for the ith line-integral, then we have for the measured line integral t_i (the collected TEC)

$$t_i = \int_{p_i} G(r,\phi)ds , \quad i = 1,2,3,,,Np, \qquad (D.6.1)$$

[33] Raymund, T.D., Ionospheric tomography algorithms, *International Journal of Imaging Systems and Technology, 5, 75-85*, 1994

[34] Raymund, T.D., Comparisons of several ionospheric tomography algorithms, *Ann Geo, 13*, 1254-1262, 1995

[35] Censor, Y, Finite series-expansion reconstruction methods, *Proc IEEE, 71*, 409-419, 1983

where P is the number of paths. We employ a finite-series expansion using N_b basis

functions $b_j(r,\phi)$ to describe the function G,

$$G(r,\phi) \approx \sum_{j=1}^{N_b} x_j b_j(r,\phi) ds = \sum_{j=1}^{N_b} x_j \int_{p_i} b_j(r,\phi) ds = \sum_{j=1}^{N_b} D_{ij} x_j \; , \qquad \text{(D.6.2)}$$

where $D_{ij} = \int_{p_i} b_j(r,\phi)$, and x_j are the weighting factors for each b_j.

Inserting this into (D.6.1) results in:

$$t_i = \sum_{j=1}^{N_b} D_{ij} x_j \qquad \text{(D.6.3)}$$

and in matrix notation:

$$\vec{T} = \overset{\leftrightarrow}{\mathbf{D}} \vec{X} \qquad \text{(D.6.4)}$$

For this work the image area is divided into pixels which are related to the set of

N_b basis functions according to,

$$b_j(r,\phi) = \begin{cases} 1, \text{if } (r,\varphi) \text{ is inside the jth pixel} \\ 0, \text{otherwise} \end{cases} . \qquad \text{(D.6.5)}$$

In this case, N_b becomes the number of pixels and the weighting factors x_j represent the

electron density in the jth pixel.

The task is now to solve (D.6.2), where the array X contains the unknown

electron density values, the array T contains the measured TEC values, and the matrix D

can be determined by evaluation of the ray path and pixel geometry. The iterative

technique chosen for this work is a modified version of the row-action method known

as the algebraic reconstruction technique (**ART**). At each iteration k in this method, the

difference between the measured values of T and the computed values of T^k is

calculated using the current solution for X^k. This difference is used to obtain a

correction to X^k, and this correction leads to X^{k+1}. After many iterations the corrections

become insignificant and the interim solutions converge to a final solution for the

matrix X.

$$X^{k+1} = X^K + \lambda_k \left[\frac{t_i - \sum_{j=1}^{Nb} D_{ij} x_j^k}{\sum_{j=1}^{Nb} D_{ij} D_{ij}} \right] D_i \qquad \text{(D.6.6)}$$

where D_i is the ith row of D, $i=k \bmod N_p$, and λ_k are relaxation parameters, in this case

taken to be the same value for all k.

The ART requires a starting point for the electron density map X to start the

iteration sequence. Two approaches to form the initial map were used in this work. A

Chapman model was fit to the collected TEC data, and used both to determine the

absolute value of the TEC and as a source for the electron density map in the algorithm.

Another approach was to use the data from the ISR (described in section E), when

available, to determine the absolute value of TEC and to generate the initial electron

density map for the ART algorithm.

E. Experimental Method: Incoherent Scatter Radar

The tomographic approach used in this work makes use of empirical supplementary data to alleviate the limited-angle problem. The Arecibo Observatory includes an incoherent scatter radar (**ISR**) which provides the vertical profile of electron density. The incoherent (or Thomson) scatter technique takes advantage of the fact that electrons scatter electromagnetic waves. The scattering cross section, $\sigma_e = 4\pi r_e^2$, where r_e is the effective electron radius, is extraordinarily small, on the order of 10^{-28} m^{-2}, but modern radar technology has made detection of the scattered signal possible. Since the ionosphere is a plasma medium and not a simple electron gas, both the spectrum and the amplitude of the scattered signal are complicated by the interaction of the electrons with the constituent ions.

The received power is given by [25]

$$\rho_r = \frac{C\sigma N \rho_t a}{R^2},$$ (E.1.1)

where N is the electron density, σ is the effective scattering cross section, a is the antenna aperture, ρ_t is the transmitted power, and C is a calibration factor which takes into account such things as feed losses, side lobes, and local geometry.

The effective cross section is given by

$$\sigma = \frac{\sigma_e}{\left(1 + \dfrac{T_e}{T_i}\right)},$$ (E.1.2)

where σ_e is the Thompson scatter cross section, T_e is the electron temperature, and T_i is the ion temperature.

The ratio of received power to transmitted power can then be given by

$$\frac{\rho_r}{\rho_t} = \frac{CaN\sigma_e}{R^2\left(1+\frac{T_e}{T_i}\right)}.$$

(E.1.2)

This illustrates the dependence of the received power on both the electron density and the electron-ion temperature ratio. Since ionospheric modification makes changes in both of these quantities, additional analysis is required. Traditionally, the spectrum and the autocorrelation function of the received ISR signal have been used to obtain estimates of T_e/T_i, but this is complicated by the complex nature of that spectrum due to wave-particle interactions and the disturbances created during ionospheric heating. [36]

ISR electron density profiles can be calibrated from either the known characteristics of the radar system, requiring detailed determination of the calibration factor C, or by comparison with to f_oF_2 (the frequency associated with the maximum electron density in the ionosphere's F_2 layer) which can be accurately determined by a nearby ionosonde. The ISR data used in this report has been calibrated using the latter technique.

---

[36] Buneman, O., Scattering of radiation by the fluctuations in a nonequilibrium plasma, *J. Geophys. Res., 67*, 2050, 1962

F. Theoretical Method: Modified SAMI2 Ionospheric Model

F.1 The SAMI2 model

The ionospheric model used in this work is one that has been developed at the Naval Research Laboratory (NRL) by Dr.s Joe Huba and Glenn Joyce, and is known as SAMI2 is Another Model of the Ionosphere (SAMI2). SAMI2 models the mid and low-latitude ionospheric plasma along geomagnetic flux tubes extending from the northern hemisphere to the southern hemisphere, using an offset tilted dipole coordinate system. These flux tubes are considered equipotentials.[37]

SAMI2 solves the ion continuity and momentum (including ion inertia along the field line) equations for seven ion species (H+, He+, N+, O+, N2+, NO+, and O2+) and electrons, and the thermal balance equations for H+, He+, O+, and electrons.

Ion Continuity Equation

$$\frac{\partial n_i}{\partial t} + \nabla \cdot (n_i V_i) = P_i - L_i n_i \tag{F.1.1}$$

Ion Momentum Equation:

$$\frac{\partial V_i}{\partial t} + V_i \cdot \nabla V_i = \frac{1}{p_i} \nabla P_i + \frac{e}{m_i} E + \frac{e}{m_i c} V_i \times B + g - \nu_{in}(V_i - V_n) - \sum_j \nu_{ij}(V_i - V_j) \tag{F.1.2}$$

Electron Momentum Equation:

$$0 = \frac{1}{n_e m_e} \nabla P_e - \frac{e}{m_e} E - \frac{e}{m_e c} V_e \times B \tag{F.1.3}$$

Ion Temperature Equation:

[37] Huba, J.D., Joyce, G., Fedder, J. A., Sami2 is Another Model of the Ionosphere (SAMI2): A new low-latitude ionosphere model, *J. Geophys. Res., 105,* 23035-23053, 2000

$$\frac{\partial T_i}{\partial t} + V_i \cdot \nabla T_i + \frac{2}{3} T_i \nabla \cdot V_i + \frac{2}{3 n_i k} \nabla \cdot Q_i = Q_{in} + Q_{ii} + Q_{ie} \qquad \text{(F.1.4)}$$

Electron Temperature Equation:

$$\frac{\partial T_e}{\partial t} - \frac{2}{3 n_e k} b_s^2 \frac{\partial}{\partial s} k_e \frac{\partial T_e}{\partial ds} = Q_{en} + Q_{ei} + Q_{phe} \qquad \text{(F.1.5)}$$

The ionospheric plasma is taken to be charge neutral, and so the electron density is equal to the sum of the ion densities. SAMI2 incorporates twenty-one chemical reactions, along with recombination between the electrons and all seven ion species. These reactions provide the loss and production terms in the ion continuity equations. The neutral species are specified using the empirical models NRLMSISE00 and HWM93.

F.2 Theoretical Approach to Ionospheric Heating

A two-stage approach has been used. Initially, an iterative method was implemented by assuming a Gaussian-shaped electron heating profile (consisting of heating intensity and vertical extent), running the modified SAMI2 using that profile, and comparing to the ISR-derived measured temperature profile. The heating profile was then iterated until the modeled temperature was in close approximation to the ISR electron temperature results. This heating profile serves to model the bulk ohmic heating that takes place during high-power HF experiments. It was necessary to modify the SAMI2 source code to include this heating profile. Tracking code was developed which would locate the altitude at which the local electron density matches a

parameterized density value. For this work, two different density matching schemes were investigated. Initially, the density parameter was set equal to the density value obtained by using the ionospheric plasma frequency, given by:

$$f_p = \left(\frac{N_e e^2}{2\pi \varepsilon_0 m_e} \right)^{\frac{1}{2}}$$

(F.2.1)

For the HF heating frequency used in this experiment, 3.15 MHz, the associated matching density is 1.24 electrons/cm^3. Using this value resulted in "burn through", in which the density cavity which is formed due to the ohmic heating reduces the maximum electron density value below 1.24 electrons/cm^3, leading to a cessation of heating for even modest values of energy input. This effect is also is observed in the ISR data, Figure 14, in which the local electron density at the center of the cavity is less than 1.24 electrons/cm^3. This burn through was ameliorated by matching the upper hybrid frequency of the ionospheric plasma, given by:

$$f_{uh}^2 = f_p^2 + \left(\frac{eB}{2\pi mc} \right)^2$$

(F.2.2)

This results in a matching density of 1.14 electrons/cm^3, and removed most of the burn through occurrences. The additional heat due to the high power HF transmissions was then applied in a Gaussian shape with a half-width of 60 km, chosen based on the ISR results.

In order to model the effect of the fast, non-thermal electrons that are generated in the nonlinear interaction of the HF wave and the plasma, changes were made to the ion-molecular charge exchange chemical reaction rates, in particular the

$N_2 + O^+ = NO^+ + O$ reaction, which depends strongly on the vibrational temperature of the nitrogen molecule.[38] Higher energy electrons (~2-3 eV), such as those created by nonlinear acceleration processes associated with high power HF heating, have a significantly greater cross section to excite the vibrational modes of the nitrogen molecule. The increased vibrational temperature of the nitrogen molecules increases the cross section of the reference charge exchange reaction, resulting in an increased ratio of nitrous oxide ions to oxygen ions. Nitrous oxide ions have a recombination rate with electrons several orders of magnitude larger than oxygen ions, so increasing the vibrational temperature of the nitrogen molecules has a net result of increasing the overall electron-ion recombination rate during heating experiments. This vibrational temperature is not currently represented in the SAMI2 chemistry code, and so a alternative method has been devised. It was decided to directly modify the ion-molecular exchange rate in the affected volume during heating. This was chosen in part in order to maintain the appropriate N_2, O^+, NO^+, and O concentration ratios. A parameter was introduced into the SAMI2 code which varies the ion-molecular charge exchange rate of the $N_2 + O^+ = NO^+ + O$ reaction in the interaction region, using the same tracking and matching code described previously.   This parameter represent the increase of the molecular nitrogen's vibrational temperature relative to it's thermal temperature. The oxygen ion charge exchange reaction rate is strongly dependent on the both the values and the ratio of these temperatures. The results, and lessons learned, of this theoretical modeling is discussed in section K.

---

[38] Milikh, G. M., Role of chemical effects in the formation of electron concentration depletions during HF heating of the ionosphere, *Journal of Atmospheric and Terrestrial Physics, 52,* 119-123, 1990

G. Phenomenon being Investigated: Large –Scale Artificially Generated Ionospheric Cavities

G.1.

High-power, high-frequency (HF) ionospheric modification facilities have been developed over the last thirty years and used to investigate the ionosphere by exciting a wide range of nonlinear responses in the ionospheric plasma. HF ionospheric modification experiments have been performed at facilities in Russia (Sura) (?), Norway (EISCAT) (?) and the US (Arecibo, HIPAS, HAARP) (?), using high-power HF antenna array systems. These systems have Effective Radiated Powers (ERP) ranging from just under 80 MW to over 1200 MW. These experiments have demonstrated the capability to generate electron density cavities via resonant electron heating in the F-region with scale lengths of tens of kilometers in the horizontal direction and hundreds of meters in the vertical direction. A generalized schematic of HF heating is shown in Figure 6. Under optimal conditions, experimenters at Arecibo have been able to create large-scale structures with estimated electron depletion levels of greater than 40%. For the heating facility at Arecibo Observatory, these optimal conditions are associated with an ionosphere having a low density ($f_0F_2 \leq 5$ MHz) and low neutral wind speeds, and can typically be found during solar minimum.

Several processes play key roles in producing these large-scale cavities. The high-power HF wave interacts resonantly with electrons at the altitude where the local plasma frequency matches the HF frequency and raises the electron temperature from

800° K to well above 2500° K. [39, 40] This increased temperature raises the pressure in the interaction region and consequently produces a magnetic-field-aligned flow of electrons out of the heated volume. [41] Also, electrons which have been accelerated by multiple reflection point crossings [42] increase the recombination rate via a two-step chemical process. These fast electrons (with effective temperatures greater than 2 eV), increase the vibrational temperature of molecular nitrogen. This in turn results in an increased ion-molecular exchange of nitrogen and ionic oxygen. The NO^+ ions then quickly undergo dissociative recombination which results in a diminished electron density.[43] Additionally, the cavity formed by these processes, in a phenomenon known as self-focusing, acts as a converging lens that focuses the high-power HF wave, whereby the EM field strength is increased and all of the formation processes are enhanced. [44] In addition, there are physical processes in the interaction between the high-power HF wave and the ionospheric plasma that result in small-scale structuring

[39] Mantas, G.P., H.C. Carlson, C.H. LaHoz, Thermal response of the F region ionosphere in artificial modification experiments by HF radio waves, *JGR, 86*, 561-574, 1981

[40] Djuth, F.T., B. Thidé, H.M. Ierkic, M.P. Sulzer, Large F region electron-temperature enhancements generated by high-power HF radio waves, *Geophys. Res. Lett., 14*, 953-956, 1987

[41] Carlson, H.C., V.B. Wickwar, and G.P. Mantas, Observations of fluxes of suprathermal electrons accelerated by HF excited instabilities, *J. Atmos. Terr. Phys., 44*, 1089-1100, 1982

[42] Grach, S.M., N.A. Mityakov, V.Yu. Trakhengerts, Electron acceleration in the prescence of parametric heating of a bounded layer of plasma, *Radiophys. Quantum Electron. Engl. Transl., 27*, 1096-1101, 1984

[43] Gennady Milikh, ibid., *Journal of Atmospheric and Terrestrial Physics, 52,* 119-123, 1990

[44] Bernhardt, P.A., et. al.,The ionospheric focused heating experiment, *J. Geophys. Res., 100*, 17331-17345, 1995

that is not discernable by the differential phase technique at UHF/VHF frequencies. [45, 46]

[45] Gurevich, A.V., T. Hagfors, H. Carlson, A.V. Lukyanov, and K.P. Zybin, Electron temperature measurements by incoherent scattering in the presence of strong small scale temperature irregularities, *Phys. Lett. A*, 246, 335-340, 1998

[46] Kelley, M.C., T.L.Arce, J. Salowey, M. Sulzer, W.T. Armstrong, M. Carter, and L.M. Duncan, Density depletions at the 10-m scale induced by the Arecibo heater, *J. Geophys. Res., 100*, 17367-17376, 1995

H. Description of Experiment

In January of 1998, nine Magnavox Model 1502 receivers were deployed on the island of Puerto Rico by the Naval Research Laboratory. The TEC data from these receivers, along with data from a separate Caribbean receiver chain, maintained by the Applied Research Laboratory (University of Texas at Austin), were used to form two-dimensional images of electron density via the technique of computerized tomographic inversion. The locations were chosen such that they formed three chains each consisting of three collinear sites along a separate meridian. This arrangement maximizes the likelihood of an intersection between the satellite-receiver sightlines and the HF-heated volume. The CIT receiver sites included a university, a high school, National Guard bases, Civil Defense sites, and the homes of several Arecibo Observatory (**AO**) researchers. Figure 7 is a table that lists these sites and provides location details. The primary criterion in choosing a site is ensuring that there are few obstructions which would interfere with VHF/UHF satellite signal reception. In addition, all sites in a given chain should be both collinear and parallel to the ground track of the beacon satellites. This is difficult in practice, and a slight variance from co-linearity for the available receiver sites must be tolerated.

Once the receivers were deployed and operational, a series of experiments were performed at the Arecibo Observatory. For each prospective satellite pass, the HF heater was turned on at full power (80 MW ERP) for a period extending from thirty minutes before the pass to just after the satellite had passed beyond the horizon. The CIT receivers collected the differential phase data (which is converted to TEC in post-

processing) while the ISR collected high-resolution information on the vertical profile of electron density.

Figure 8 is a map of the island of Puerto Rico, and indicates the locations of each site, the location of the HF heater, and the location of the AO ISR. Note that the receiver sites are distributed across the island, and that one site is very near the HF heating facility. Also note that the HF heating facility is not co-located with the ISR, but is on the northern coast, approximately 15 km from the ISR. Figure 9 is an isometric view showing an idealized satellite flyover, and demonstrates the three reconstructions planes associated with the distributed receiver array.

I. Experimental Results

I.1. Satellite Overflight

Figure 10 indicates the island boundary with a thin black line and indicates the Arecibo heater location by a green spot. The size of the green spot is intended to depict the size of the HF transmitter beam as estimated for 350 km altitude, which is the approximate altitude of the F layer of the ionosphere. Also depicted is the ground track of the satellite (asterisk.) Each of the three other tracks (diamond, plus, triangle) represents the intersection of one plane, defined by the satellite pass and a specific ground receiver, and a second plane defined by 350 km altitude. This intersection is the "350 km altitude track" of the satellite along the ground receiver's line of sight. The diamond (triangle) symbols identify the "350 km altitude track" of the westernmost (easternmost) receiver chain. Note that the triangles intersect the middle of the green spot and the plusses intersect the edge. Since the diamonds do not intersect the green spot, the signal from the westernmost chain would be expected to be unaffected by the heating.

I.2. TEC measurements

Figure 11 shows the latitudinal profile of TEC for each of the seven receivers. Each profile is compiled for the satellite pass DOY 027, 1998, 0337 UT, and is arranged to coincide with the relative position of the receiver with respect to the silhouette of the island of Puerto Rico. Figure 12 is the same TEC data after passing through a ten second smoothing filter. This process is known as de-trending and it eliminates the U-shaped curve in the slant TEC data that is due solely to geometric factors while

highlighting any other structure present in the data. Note that the profiles associated

with the westernmost receiver chain (chain A) are relatively free of structure, i.e.

approximately corresponding to a $\sec(\chi)$ relationship (χ being the zenith angle),

compared to the profiles associated with the easternmost chain (chain C). This is

expected since the line of sight for chain A encounters only the unmodified ionosphere

whereas the line of sight for chain C passes through the heated region. For the signals

from the center chain (chain B), slight variations in the $\sec(\chi)$ curve results from the

line of sight passing through the edge of the heated region. When these data are

analyzed tomographically, it is the variations from the $\sec(\chi)$ curves that are

responsible for the structure in the electron density map of the ionosphere. As pointed

out in section D, the TEC data is to be used for resolving the unknown TEC offset via

fitting with a Chapman model, for establishing an initial guess for the tomography

algorithm using that same Chapman model, and as part of the iterative process within

the algorithm. The fitted Chapman model, with the associated calculated TEC profile,

is shown in Figure 13 along with the measured TEC.

I.3. ISR measurements

Figure 14 is the vertical profile of electron density measured by the Arecibo

ISR. This data corresponds to the beginning of the satellite pass reconstructed in

Figures 15 and 16, occurring at DOY 027, 0337 UT, 1998. That the radar beam passes

through the heated volume can be seen by the reduction in electron density from 350

km to 410 km altitude that reaches a maximum reduction of approximately 50% at 380

km altitude. Over much of the altitude range depicted, this profile can be described by a

Chapman model. Minor deviations from the model are visible at 150 km altitude and are caused by chemical (e.g., long-lived metal ions) and physical (e.g., convective instabilities) processes which are ignored by the model. The primary deviation from a Chapman profile is the modification of ionospheric electron density by the HF heater. The plasma line artifact is observed as an apparent spike in electron density at 380 km altitude. Recall from the discussion in section E that this artifact does not represent real electron density, but does provide an indication of the height of the HF-absorption. The dashed line on the plot is a Chapman-fit to the data, and serves as the unmodified ionosphere baseline. As pointed out in section E, the ISR data is to be used both for resolving the unknown TEC offset as well as establishing an initial guess for the tomography algorithm. It is not used within the iterative tomographic process.

I.4 Tomographic Reconstructions

I.4.a Chapman-model based calculations

Figure 15(a-c) shows the tomographically reconstructed electron density maps of the ionosphere above Puerto Rico using the TEC data to both resolve the unknown offset and to generate an initial Chapman-profile guess for the tomographic algorithm. Figures 15 a, b, and c are the reconstructions for receiver chains A (westernmost), B (central) and C (easternmost) respectively. The characteristic Chapman hump in the vertical electron density profile is obvious as a horizontal band on each map. Recall that the strength of any ground-based implementation of the tomographic technique lies in resolving horizontal structure. This is particularly true when a small number of receivers are spaced over a short array baseline, as in our case. Consequently it is this

horizontal structure, particularly near the altitude of maximum electron density, that will be the focus of this discussion. Consistent with the latitudinal asymmetry visible in the TEC data in Figure 11, Figure 15a indicates a gentle rise of about 13% in maximum electron density from the southern (left) edge to the northern (right) edge of the map. No structuring beyond a percent or two is visible on the map. This same rise is visible in Figure 15b, but here can be noticed a localized electron density depression from 18.0 degrees latitude to 18.14 degrees latitude with a maximum density reduction of roughly 5%. In figure 15c, the localized depression extends half a degree in latitude and reduces the electron density by 15%. This progressive sequence in the cavity dimensions is what you would expect looking at Figures 11 and 12 which shows that evidence of the heated region should be most apparent in Figure 15c and least apparent in Figure 15a. The vertical dimension of the cavity cannot be determined due to the limited vertical resolution. Although the measurement of the horizontal structure is significantly more precise, the relationship between this measurement and the dimensions of the HF-generated cavity involves some uncertainty because it is unknown precisely which vertical planar cut of the spheroidal cavity is being sampled. Since Figure 15c shows the cavity to be at least ½ degree and since 1 degree of latitude corresponds to 118 km at the altitude in question, the horizontal diameter of the cavity is at least 50 km.

It must be recalled that each tomographic image plane is not vertical, but instead lies in the satellite path receiver site plane. This results in an altitude-longitude correlation. By mapping the longitude of the Arecibo heater to the corresponding image plane altitude, it is shown that an upper portion of the heated volume is being sampled.

Together with the magnetic-field-aligned characteristic of the cavity, this explains the apparent southward displacement of the cavity from the heater latitude in the tomographic reconstructions.

I.4.b. ISR-based reconstructions

Figure 16(a-c) shows the tomographically reconstructed electron density maps of the ionosphere above Puerto Rico using the ISR data to both resolve the unknown offset and to generate an initial vertical-profile guess for the tomographic algorithm. Figures 16 a, b, and c are the reconstructions for receiver chains A (westernmost), B (central) and C (easternmost) respectively. The ISR vertical profiles contain much better information than the TEC-based vertical profiles fit using the Chapman model for two reasons. First, the ISR profiles are determined more directly from measurements. Second the ISR profiles contain fine scale features ignored when using the Chapman model. By using direct measurements, the TEC offset is more accurate and by incorporating the fine-scale features into the initial guess, the final profile is more accurate, i.e. the paucity of vertical resolution in this implementation of tomographic analysis is somewhat compensated. These improvements that are attributed to using the ISR vertical profile allow the identification of fine-scale horizontal stratification on top of the Chapman-like hump in all three maps in Figure 16. As in Figure 15 a, b and c, Figure 15 a, b, and c shows the gentle rise in the electron density arising from the natural asymmetry in the north-south direction observed in the TEC data. The localized depressions in Figure 15 b and c appear in Figure 16 b and c with similar dimensions. In Figure 16 b, the depression is at 330 km altitude and centered at 18.2 degrees latitude

and in Figure 16 c the depression is at 330 km altitude and centered at 18 degrees

latitude. As before, this structuring suggests a lower limit to the horizontal cavity

diameter of 50 km.

J. Discussion of Experimental Results

The largest contribution to uncertainty in performing ionospheric tomographic reconstructions lies with the TEC data itself. In the ideal case, coverage of all possible ray paths are complete and continuous and the reconstruction is unique. The curvature of the Earth prevents the acquisition of data at look angles corresponding to a horizontal integration path at low altitude. The limitation of having a finite number of receivers means two things. First, the coverage of ionosphere at any one moment during the pass is limited to one line of sight for each receiver. Thus any time evolution of the structure introduces artifacts into the finalized image. Second, the deviation in the line-averaged electron density due to horizontally localized structure is a greater percentage of the TEC when the receiver is directly below the structure. At off-vertical angles, the TEC includes proportionally more non-structured ionosphere compared to structured ionosphere. In addition, the TEC value obtained by the differential Doppler method is relative TEC, and requires an external determination of the offset necessary to obtain absolute TEC. Instrument-based limitations of the phase resolution correspond to a minimal detectable TEC variation, which in this study is one part in 10^5. This limitation in detecting small changes in line integrated electron density prevents the detections of structures with vertical extent that is small, altitude that is far from the F-layer peak, and electron density deviation that is tiny. The tomographic method itself results in exact, unique solutions when the input data satisfies, or nearly satisfies, the ideal conditions.

A number of differences between this study and a recent study performed at the EISCAT facility can be described in terms of the constraints mentioned above. Both

studies use comparable numbers of receivers per chain (3 receivers per chain for the Arecibo study, and 5 receivers in a single chain for the EISCAT study), so the temporal resolution of structure evolution would likewise be comparable. However, the EISCAT receiver array was roughly 480 km in latitudinal extent while our receiver array extended less than 50 km. This configuration means that the EISCAT study had greater vertical resolution due to the long baseline for the receiver chain, while our study had greater horizontal resolution from the close spacing of receivers. Obviously, with a longer baseline for the receiver chain, the EISCAT study imaged a greater latitudinal extent. This is desirable due to the nature of both the highly variable ionosphere at high latitudes and the intense ionospheric modifications produced by the EISCAT HF heating facility.

A brief comparison of the EISCAT and the Arecibo Observatory heating facilities is in order. The EISCAT facility is located near Tromsø, Norway at the geographic coordinates 69.6^o N and 19.2^o E. The magnetic dip angle at that location is approximately 78°. The heating facility consists of twelve transmitters capable of generating a total CW power of 1.2 MW with a frequency range of 3.85-8.0 MHz, and an antenna array gain of 24 dBi. This results in a maximum effective radiative power, after losses, of 300 MW. The Arecibo heating facility is located near the town of Islote, on the north coast of Puerto Rico at geographic coordinates 18.4^o N and -66.6^o E. The magnetic dip angle is approximately 50°. The heating facility consists of 4 transmitters capable of generating a total CW power of 800 kW with a frequency range of 3.175-8.0 MHz, and an antenna array gain of 23 dBi. This results in a maximum effective

radiated power, after losses, of 80 MW. The EISCAT facility can therefore inject a significantly greater level of radio-wave energy into the ionosphere.

The work performed here has a number of possibilities for extension. Recently developed differential Doppler receiver systems are compatible with a greater number of beacon frequencies, significantly increasing the fraction of currently orbiting beacon satellites available for CIT studies. By expanding the number of satellites involved in each study, the data can be accumulated in a shorter period of time. Therefore, the high-power HF heating research community will have more opportunities to take tomographic snapshots of phenomena associated with an artificially perturbed ionosphere and the ionospheric research community as a whole will have more frequent monitoring of the behavior of the ionosphere. A number of new beacon satellites have recently been launched, with plans for even more in the near future.   Also, over the next few years it is anticipated that a number of low earth orbiting satellites will be launched that include a differential Doppler receiver as part of their payload. Receiver-equipped satellites will be able to provide horizontal integration paths which are currently unavailable. As discussed in the CIT section, horizontal integration paths contribute important information in the reconstruction algorithm.

K. Discussion of Theoretical Results

As discussed in Section F, a two stage approach was used in modeling the effects of the high power HF heater on the ionosphere. First, the ohmic heating caused by the interaction of the radio wave and the ionospheric plasma is simulated by directly introducing heat to the electrons in the region of HF absorption where the local plasma frequency is near the frequency of the impinging radio wave. Secondly, a portion of the effects of the fast, non-thermal electrons generated in the nonlinear interaction of the HF wave and the ionosphere are modeled through incorporating a simulated increase in the nitrogen vibrational energy by modifying the ion-molecular charge exchange chemical reaction rate for the reaction $N_2 + O^+ = NO^+ + O$. The location of the heated interaction region is dynamically set during each time step of the simulation to the altitude at which the local upper hybrid frequency equals the HF heater frequency specified in a parameter file.

The first step was to determine the SAMI2 input parameters which would result in an ionosphere which was as similar as possible to the observations made the night the TEC measurement occurred. A normal SAMI2 modeling run involves defining the input parameters which are used by the code to begin and then evolve the model. Typically, the model is allows to run for twenty four simulated hours, and then the results are output to data files. The parameters used in SAMI2 include the day, year, 10.7 cm solar flux, the 3-day average of the 10.7 cm solar flux, and the geomagnetic disturbance index A_p. Initially, entering values for these parameters which matched those for the night of the experiments resulted in unusual SAMI2 results. Below a

certain value of the 10.7 cm solar flux, no ionosphere would develop. Consultation

with the SAMI2 code developer, Dr. Joe Huba, led to the discovery that there was an

error in a third-party code used within SAMI2 to derive the a version of the Chapman

function which in turn drove the electron photoproduction subroutines. A new version

of SAMI2 was released, in part due to this discovery, which fixed this error and made a

few other changes to the code. This new code, when used with the parameter values

from 27 January 1998, provided an ionosphere which nearly matched observations.

However, the ion temperature was greater than that measured by the ISR (shown in

Figure 17), and so the background neutral temperature was lowered using a parameter

provided for that purpose. The undisturbed ions are in thermal equilibrium with the

background neutrals, and so the ion temperature was reduced as well. The nominal

SAMI2 model run now matched the observations.

The ohmic heating profile was chosen by matching the results of a SAMI2

simulation run with the ISR electron temperature data shown in Figure 17. After a

number of simulation runs, it became apparent that for even moderate values of heating

input, heating efficiency was actually reduced as the heating input increased. The

source code was modified to provide step-by-step diagnostic output with respect to the

various electron heating parameters, and it was discovered that a numerical instability

was occurring during the artificial heating cycle. Decreasing the time step reduced the

magnitude of the instability, and it was determined that a time step of one half second

during the artificial heating interval eliminated the instability. For comparison, the

SAMI2 nominal time step is on the order of ten seconds. Software code was introduced

to reduce the time step to one half second solely during the heating interval, in order to prevent on undue increase in the time for a model run. Consultation with Dr. Huba after implementing the change indicated that this was the correct approach.

After a number of simulation runs using this final SAMI2 code, a heating scale height of 60 kilometers and a heating intensity of 941 K/s applied to the electrons were chosen as the best fit to the temperature profile data. The charge exchange reaction rate was unmodified during these simulation runs. The results of this SAMI2 simulation are shown in Figures 18 through 22. Figure 18 is a time/altitude plot of the electron temperature above the Arecibo Observatory for a representative, non-heating run. The time is in UT, and the model was run for twenty four simulated hours prior to the displayed data in order to eliminate any early variances in the model. Figure 19 is the result of a simulation run, with the heater-on period occurring for twelve minutes, starting at 0300 hours. A twelve minute heating time was chosen due to limitations inherent in the two-dimensional constraints of SAMI2. Since we are limited to heating along a specific flux tube, non-realistic consequences occur when simulating extended heating periods. Figure 20 shows the difference in temperature between the nominal background ionosphere in Figure 18 and the heated ionosphere in Figure 19. Figures 19 and 20 demonstrate the match to the increase in electron temperature as obtained via the ISR as shown in Figure 17. Figure 21 is the nominal electron density background result using the 27 Jan 1998 ionospheric parameters. Figure 22 is the electron density during a heating simulation run at 941 Ks/, and Figure 23 shows the change in electron density due to heating, as compared to the background ionosphere shown in Figure 21.

The reduction in electron density of -5.08e4 electrons/cm^3 is less than the -5.65e4 that is observed in the temperature corrected ISR data. The difference is accounted for by recalling that the SAMI2 heating method models only the bulk, ohmic heating of the electrons due to their interaction with the high power HF electromagnetic field. The suprathermal tail of the modified electron distribution function, as described in Section F, is has been modeled by modifying the charge exchange rate associated with the $N_2 + O^+ = NO^+ + O$ reaction. Figure 24 is a plot of the maximum reduction in electron density when both the ohmic heating and the reaction rate are included, shown as a function of the rate modification factor (i.e., a modification factor of two indicates an increase in the reaction rate by a factor of two). The curve indicates that a value of the modification factor 2.02 is required to match the observed density reduction of -5.65e4 electrons/cm^3. A vibrational / translation temperature differential of 308 degrees K corresponds to the reaction rate factor of 2.02, for the translational temperatures observed during the experiments. This is in good agreement with previous theoretical heating efforts addressing the effect of the vibrational states of nitrogen on HF heating experiments[47]. The final modeling result for the electron density is shown in Figure 25, including both the ohmic heating and the chemistry effects. Figure 26 illustrates the difference between the pure ohmic heating and that which includes the chemistry modifications. The chemical effects increase the density reduction rate, and slow down the effective electron replacement rate.

---

[47] Vlasov, M. N., Kelley, M. C., Gerken, E., Impact of vibrational excitation on ionospheric parameters and artificial airglow during HF heating in the F region, *J. Geophys. Res.,109,* A09304, doi:10.1029/2003JA010316, 2004

L. Conclusion

It has been shown that the CIT technique can be applied to the three-dimensional, high-resolution imaging of artificially generated ionospheric cavities above the HF heater at Arecibo Observatory. Current geometric constraints necessitate the use of supplementary data to determine the vertical profile of electron density. CIT is used to resolve the density/temperature ambiguity in ISR measurements. The differential phase technique measures only the electron density of the ionosphere. The ISR backscatter signal, as indicated in section E, is dependent on both the electron density and the electron/ion temperature ratio. Self-consistent analysis methods can be used to determine the temperature ratio, but they are not purely empirical and require assumptions to be made about the ionosphere. By combining the TEC data with the ISR data, the effects of the temperature ambiguity are minimized.

The experimental observations were supported by theoretical work using the open-source SAMI2 ionospheric model. Methods were developed to model both the ohmic heating of the electrons and the suprathermal heating caused by nonlinear effects. Modeled ohmic heating values of 941 K/s match the observed heated temperature profiles, and an increase of the $N_2 + O^+ = NO^+ + O$ reaction rate by a factor of 2.02 results in a matched electron density reduction of 5.65e4 electrons/cm^3.

Figure 1a: Chapman theory: Geometry

Sun

s

χ

h

Earth
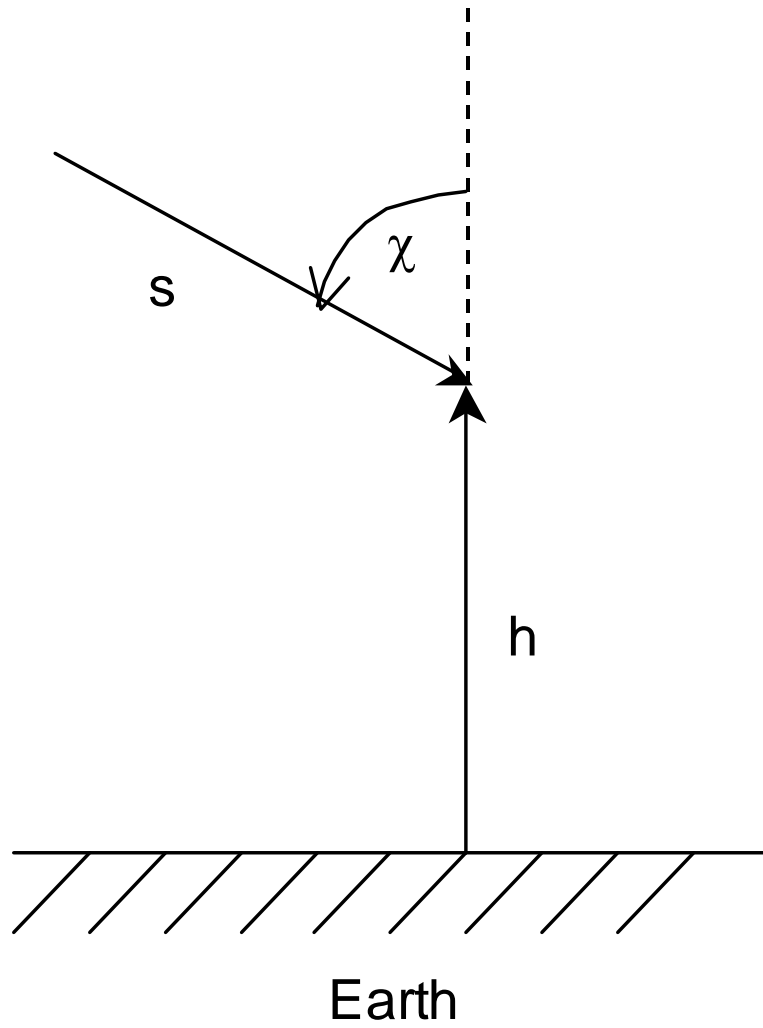
Figure 1b: Chapman theory: Hydrostatic gas and Intensity Profile
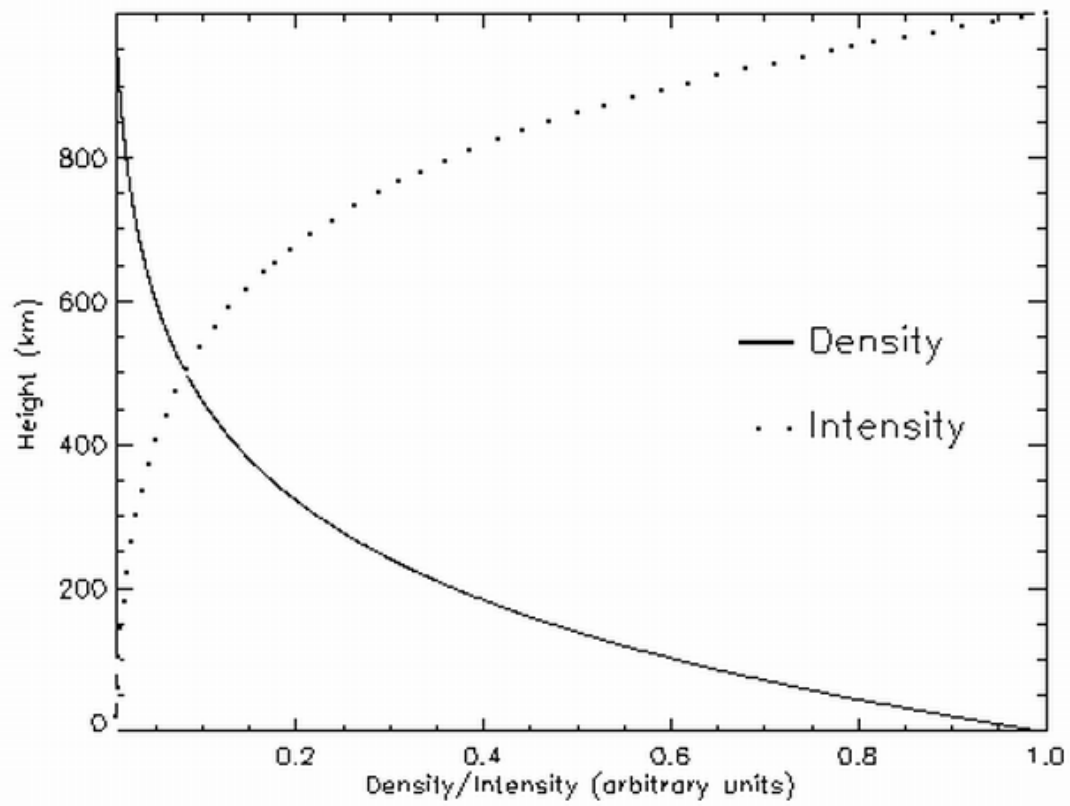
Figure 2: Chapman production example
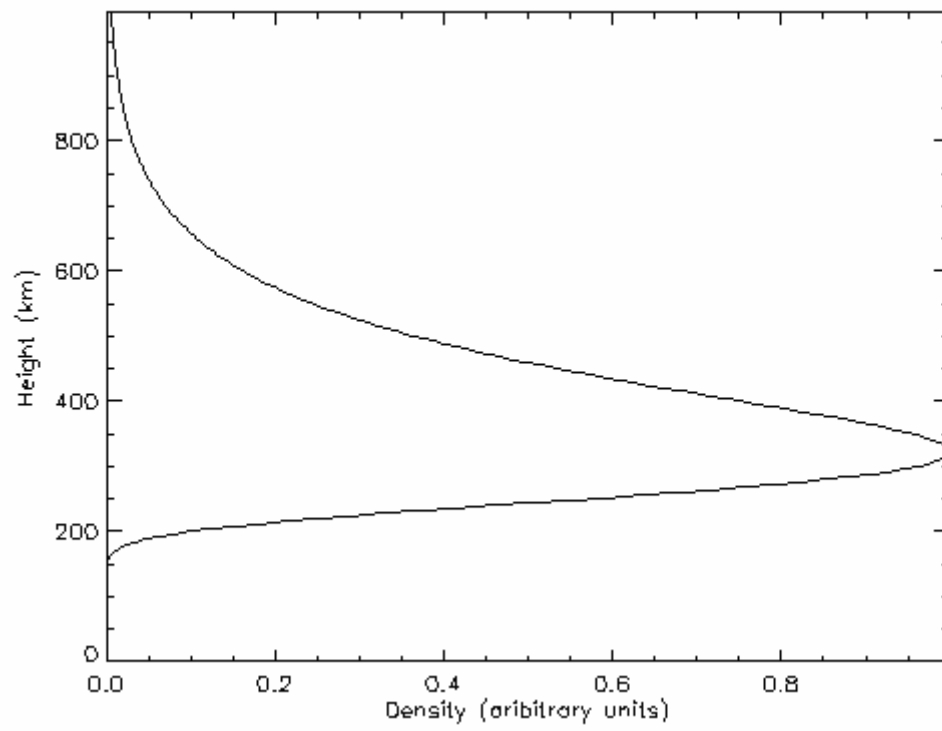
Figure 3a: 1/e Intensity Height
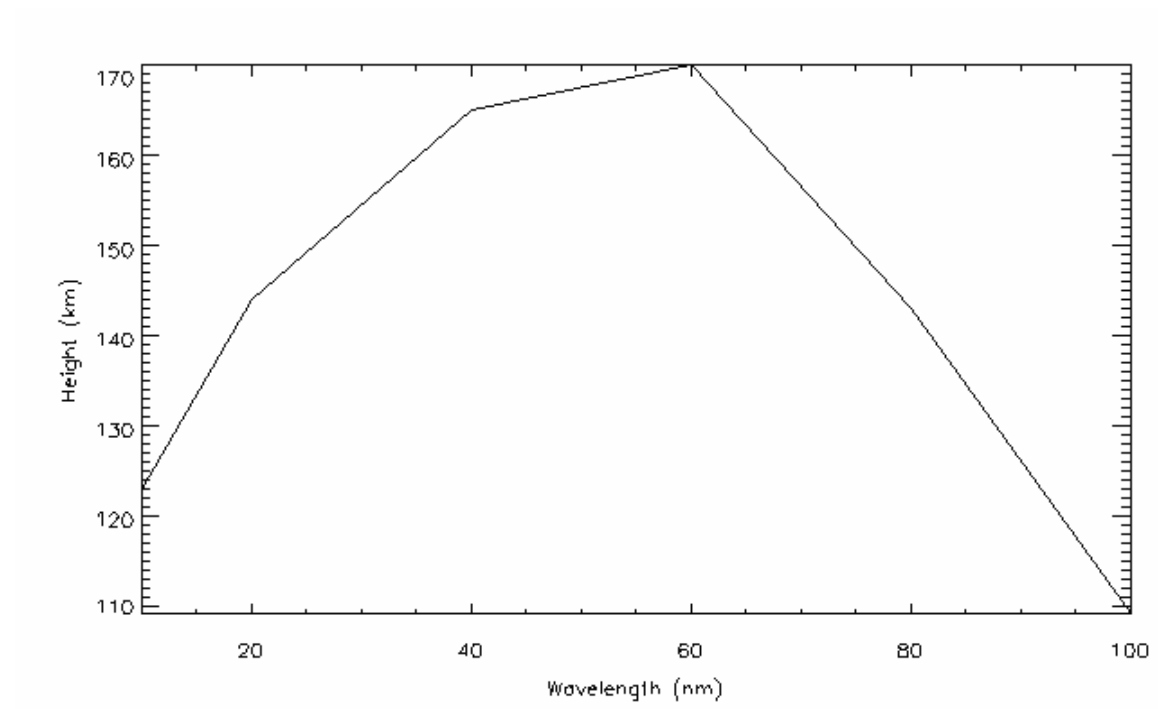
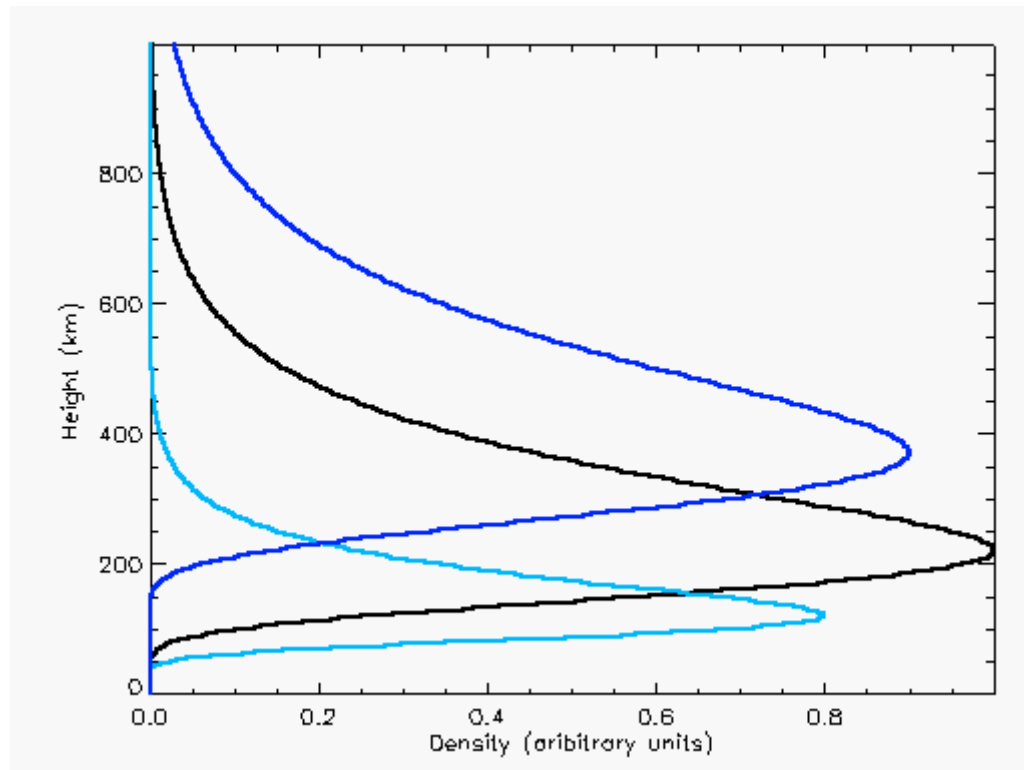Figure 3b: Multi-spectrum Chapman Examples
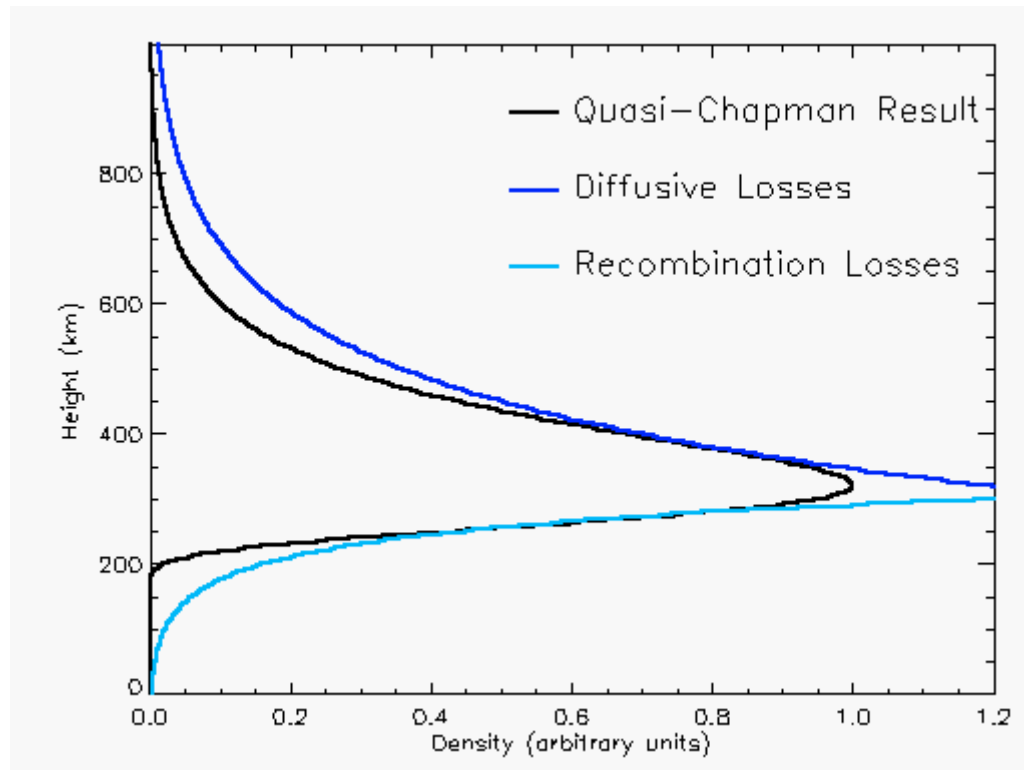
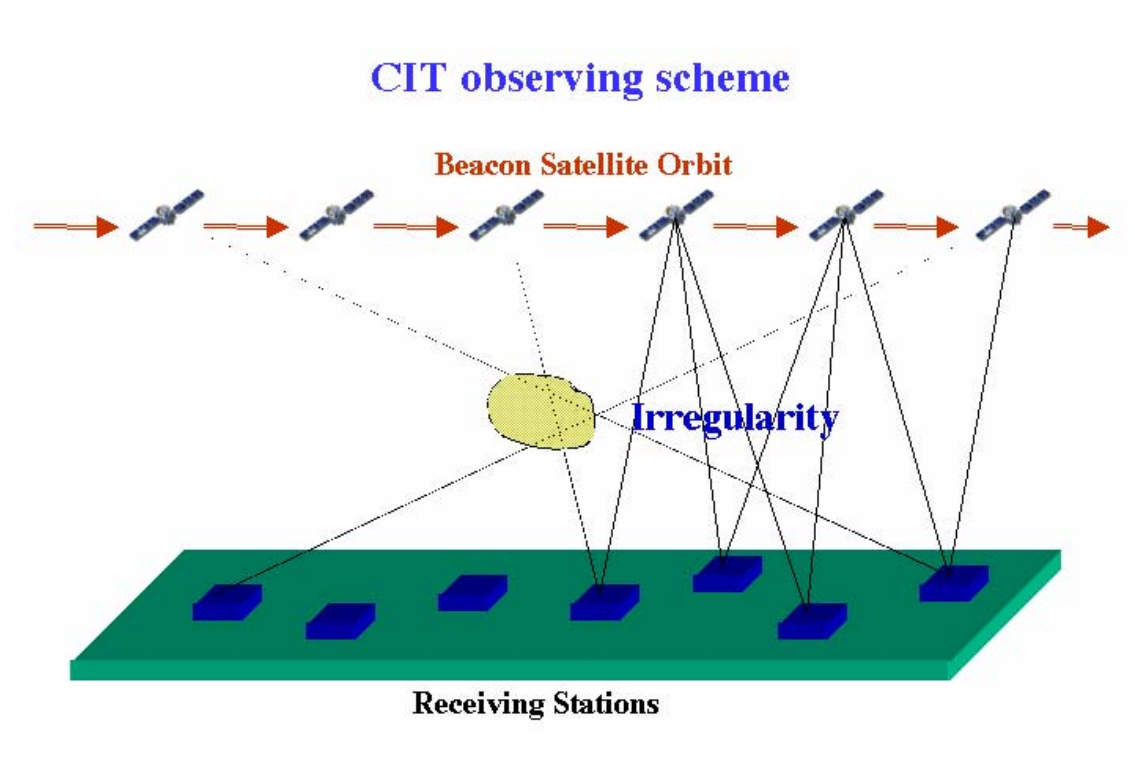Figure 4: Equilibrium profile

Figure 5: General CIT Observing Schematic

Figure 6: HF Ionospheric Modification Schematic

Figure 7: Table of site locations
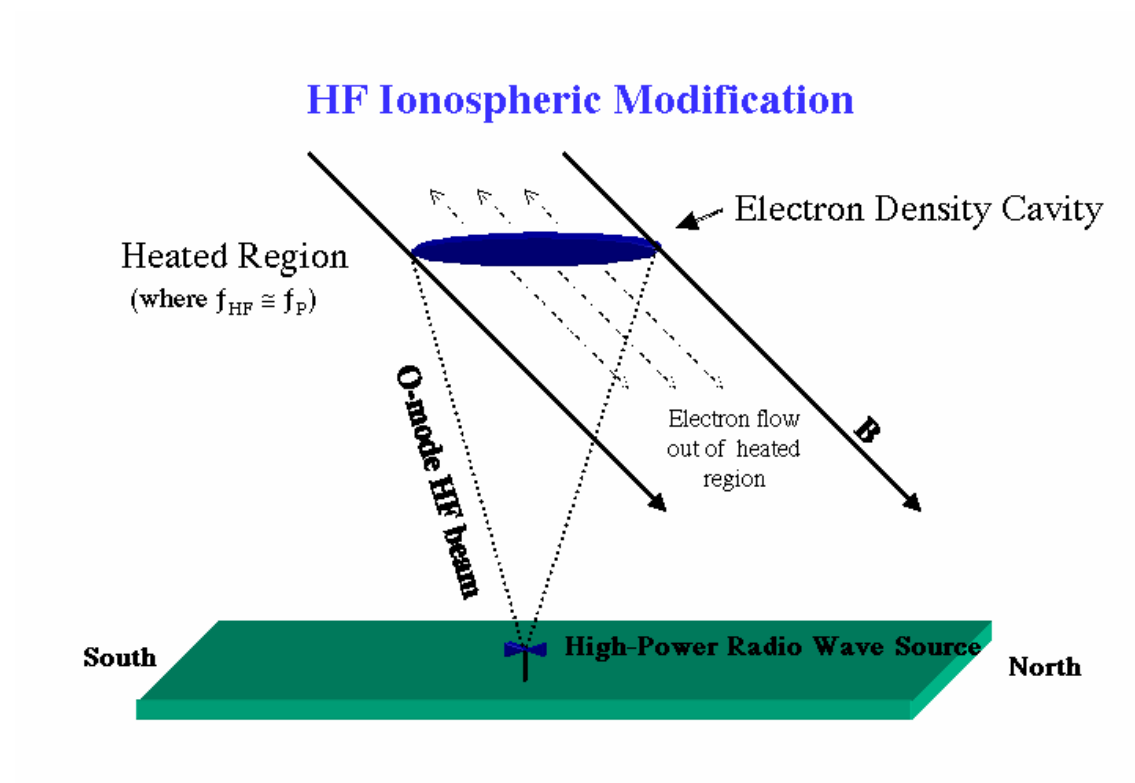
Site	Site ID	Latitude	Longitude	Chain
Ramey	2	18.39	-67.13	1
Mayaguez	10	18.09	-67.14	1
Cabo Rojo	9	17.96	-67.15	1
Islote	5	18.37	-66.64	2
Utuado	6	18.15	-66.71	2
Peñuelas	8	17.94	-66.72	2
Sabana Seca	53	18.38	-66.17	3
Cidra	1	18.06	-66.16	3
Guayama	7	17.86	-66.11	3
Bermuda	55			4

Figure 8: Arecibo 98 Receiver Deployment

Arecibo 1998 CIT Receiver Deployment

Figure 9: Idealized Observing Schematic
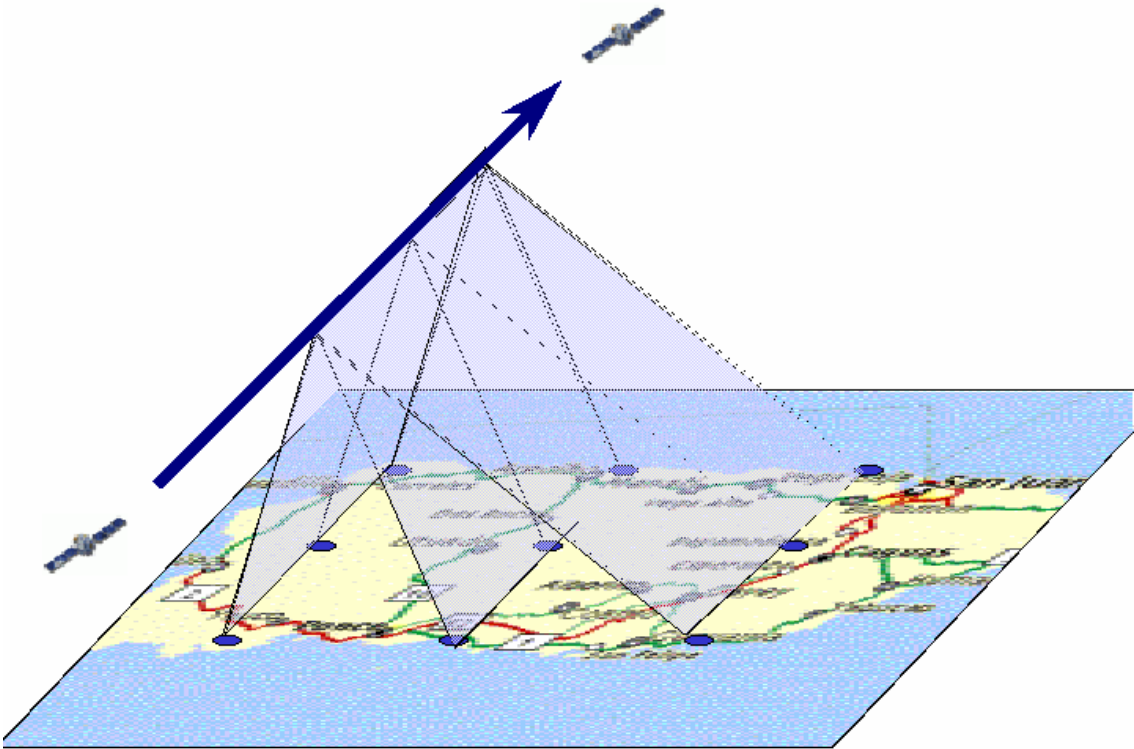
Figure 10: Satellite Overflight

Satellite Overflight and Heater Location
DOY 027, 1998, at 03:37 UT

North

Arecibo HF Heater location

* Satellite ground track
◊ Western Chain F-region intercept
+ Central Chain F-region intercept
△ Eastern Chain F-region intercept

Figure 11: Slant TEC

Slant TEC - DOY 027, 1998, at 03:37 UT
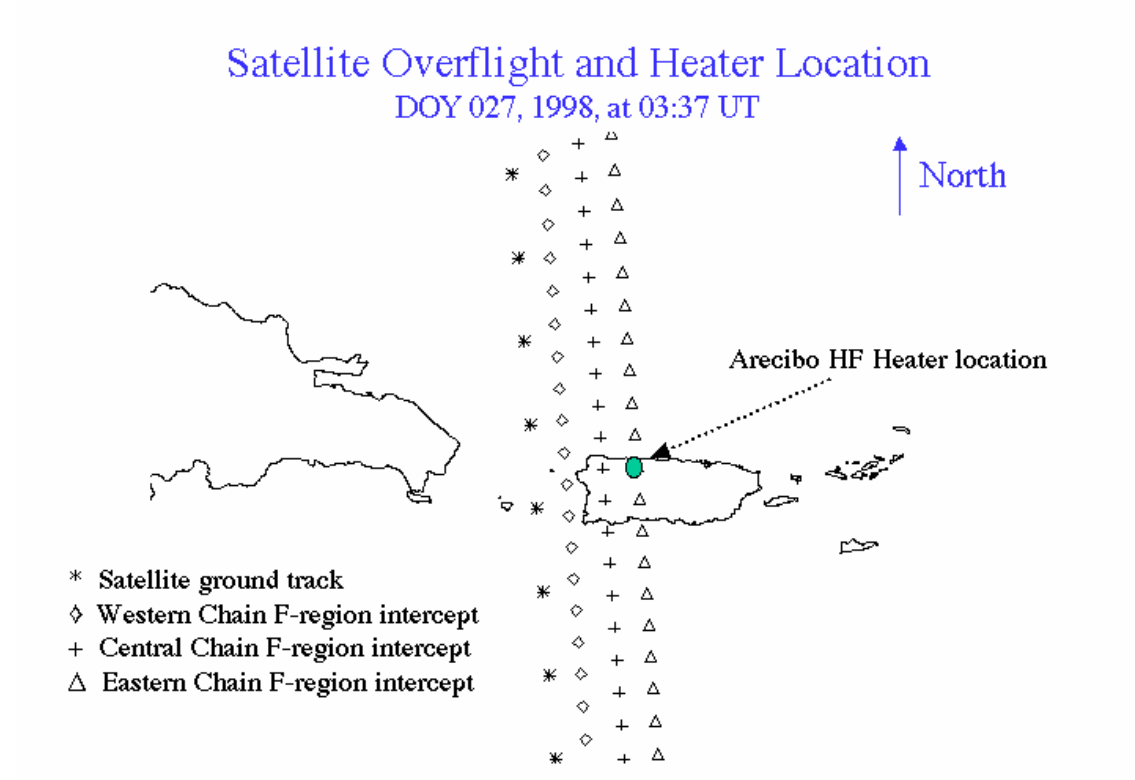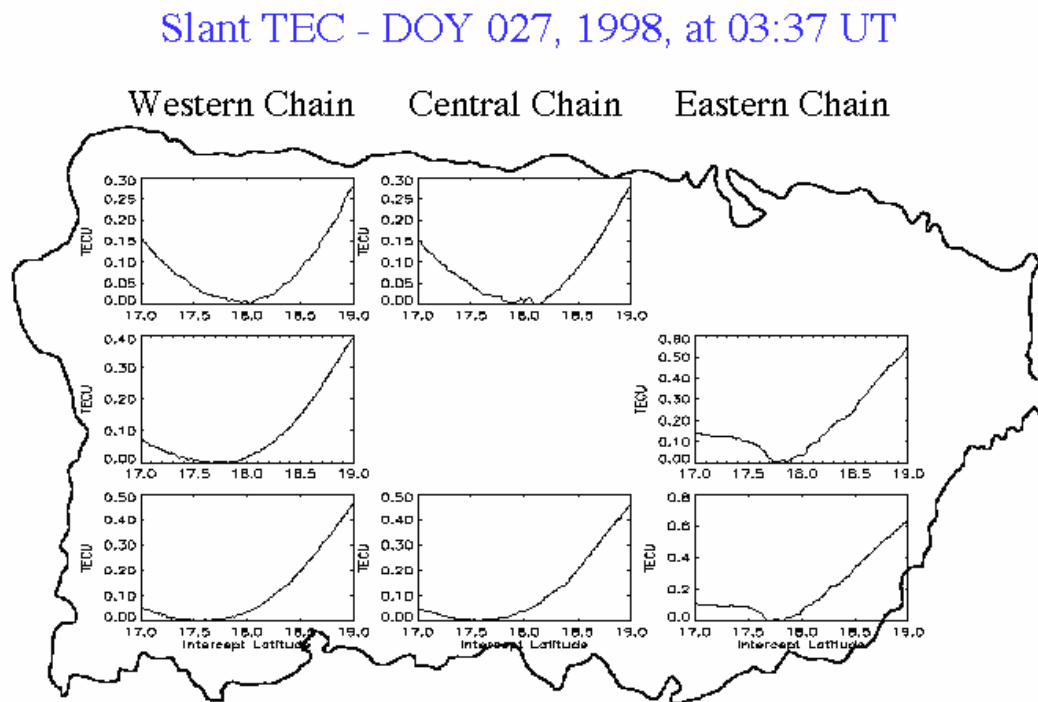
Figure 12: Detrended TEC
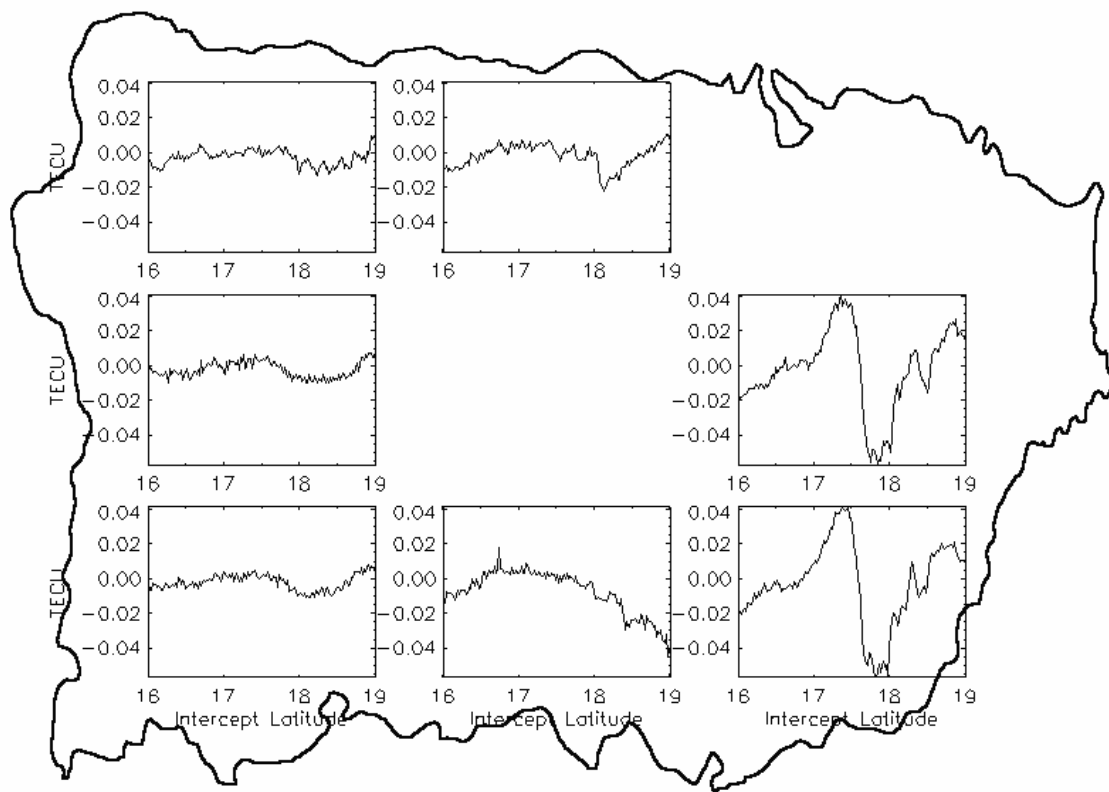
Figure 13: Chapman Model and Fit

Figure 14: ISR Radar Data

27 January 1998, 0337:00 AST
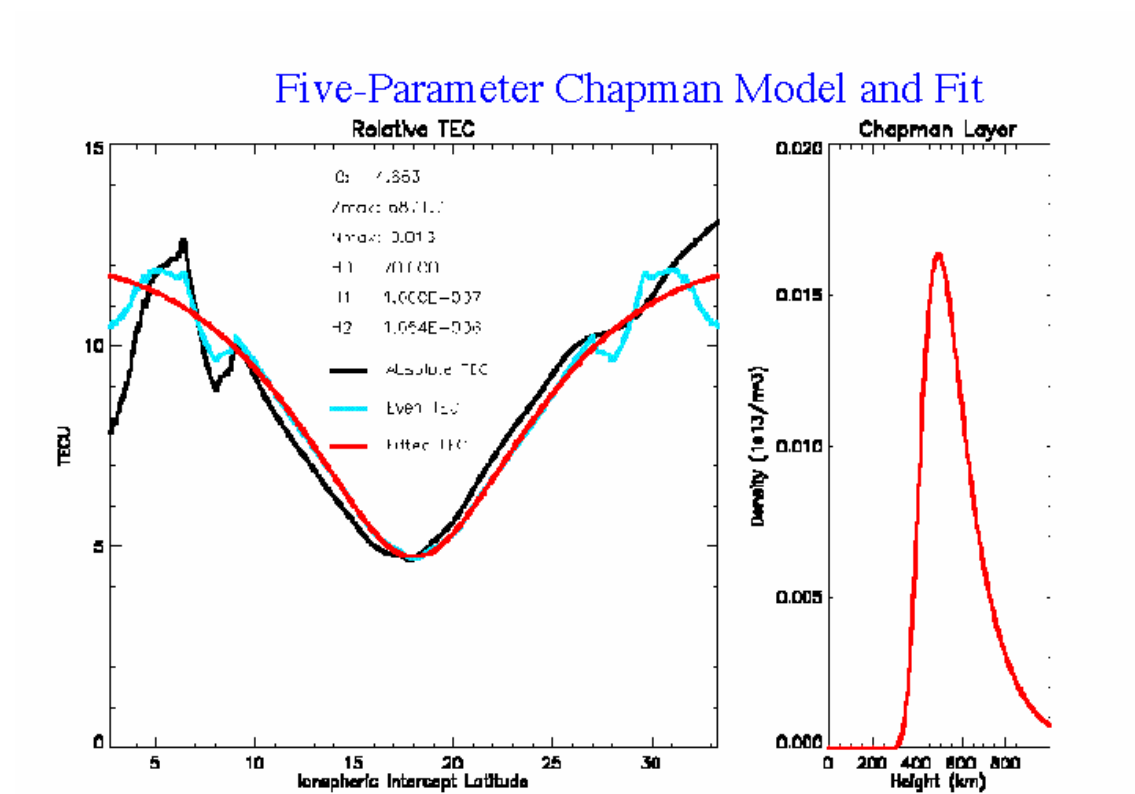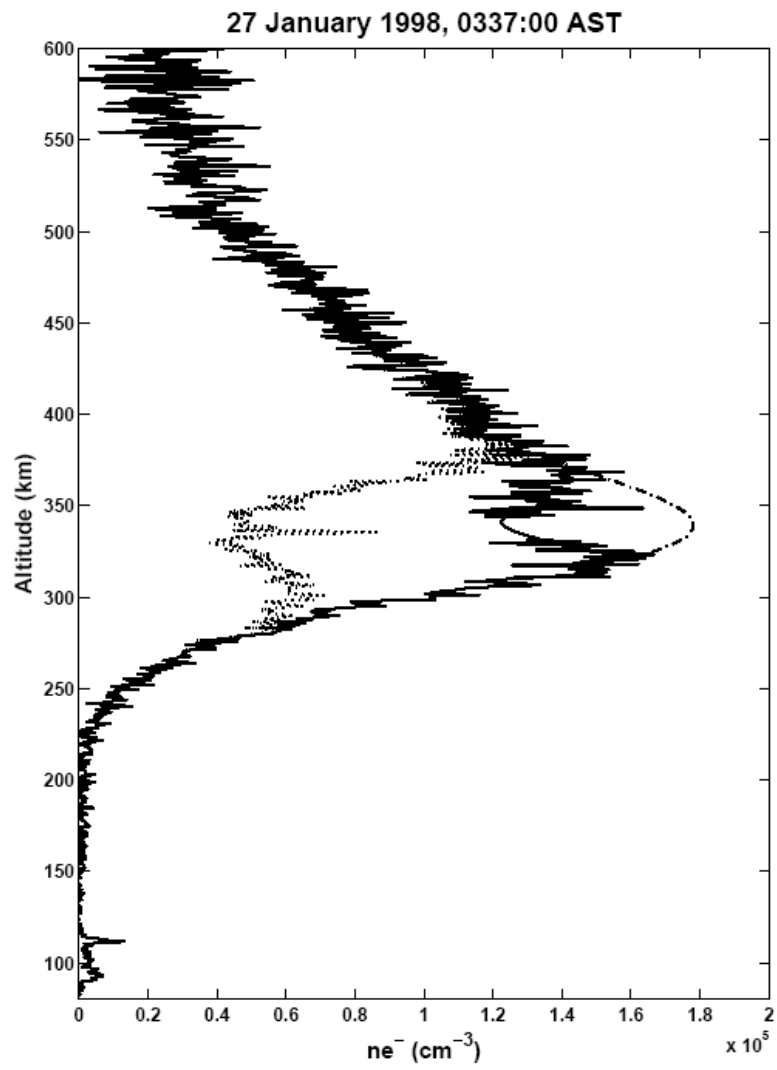
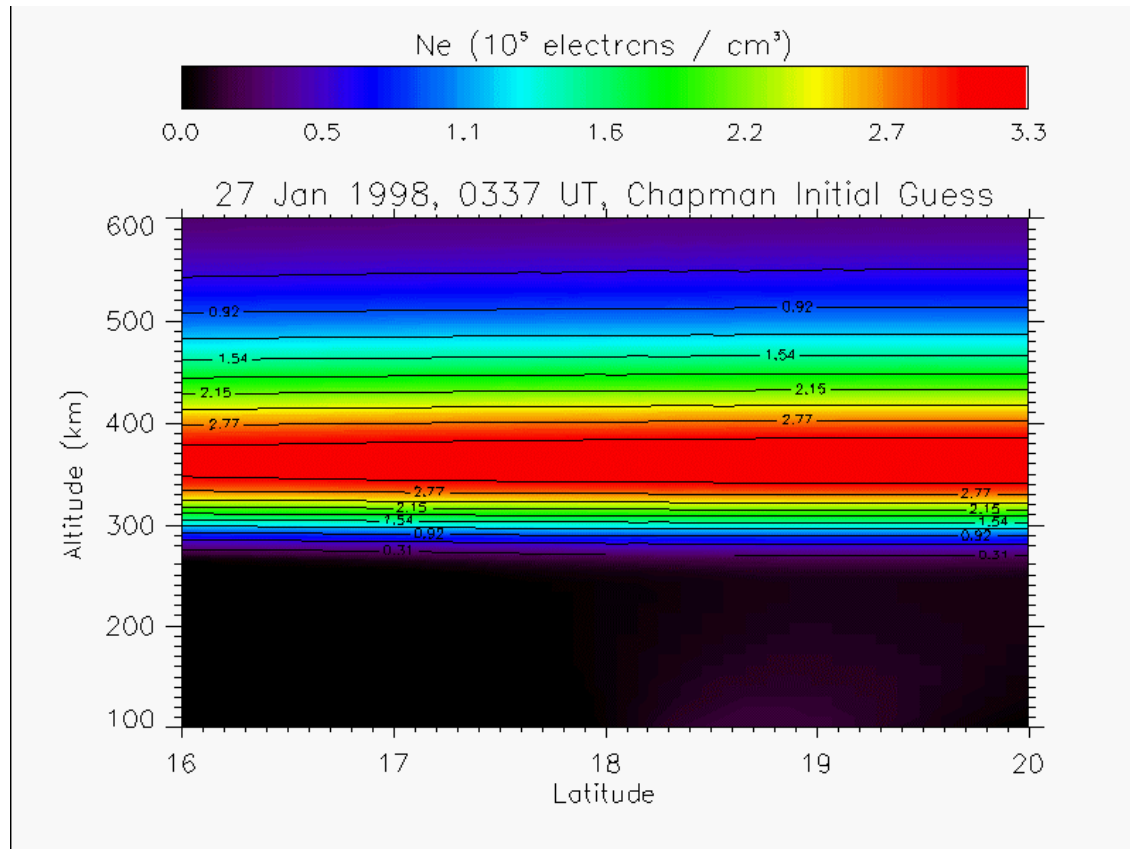Figure 15a: Western Chain Reconstruction, Chapman Initialization

Figure 15b: Central Chain Reconstruction, Chapman Initialization
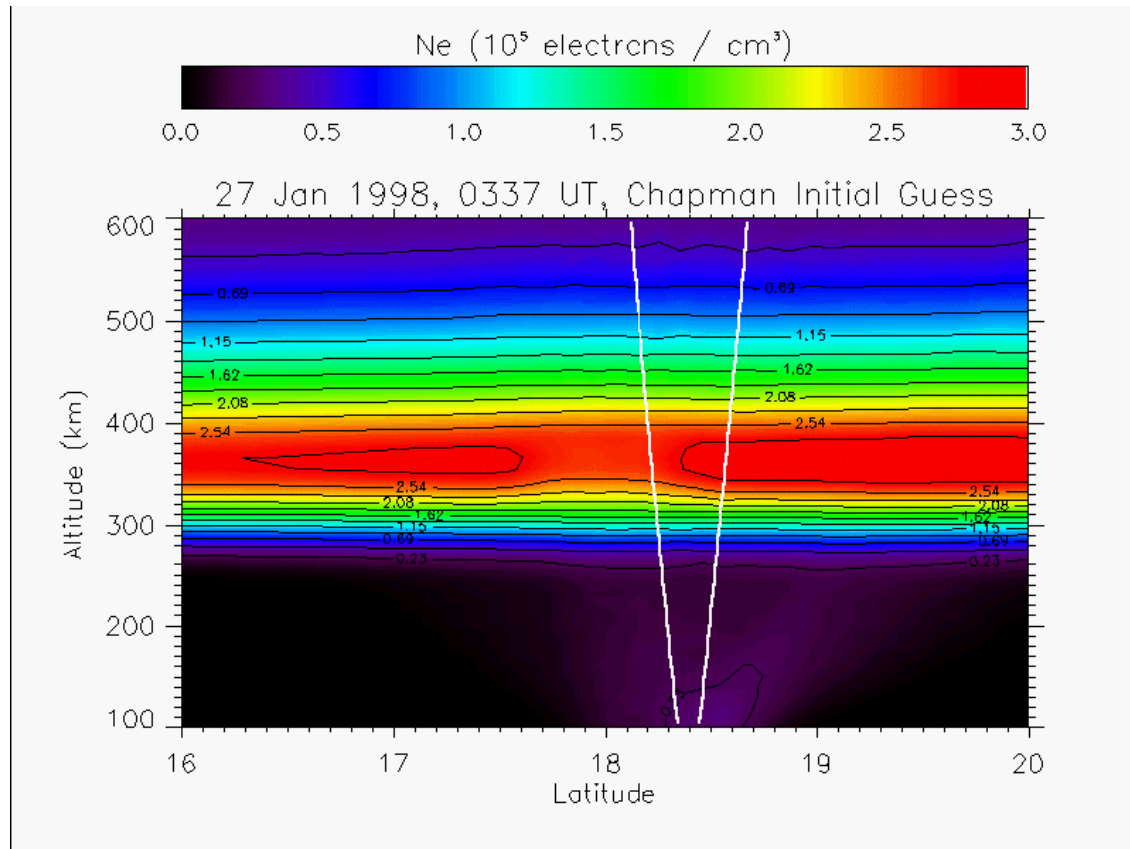
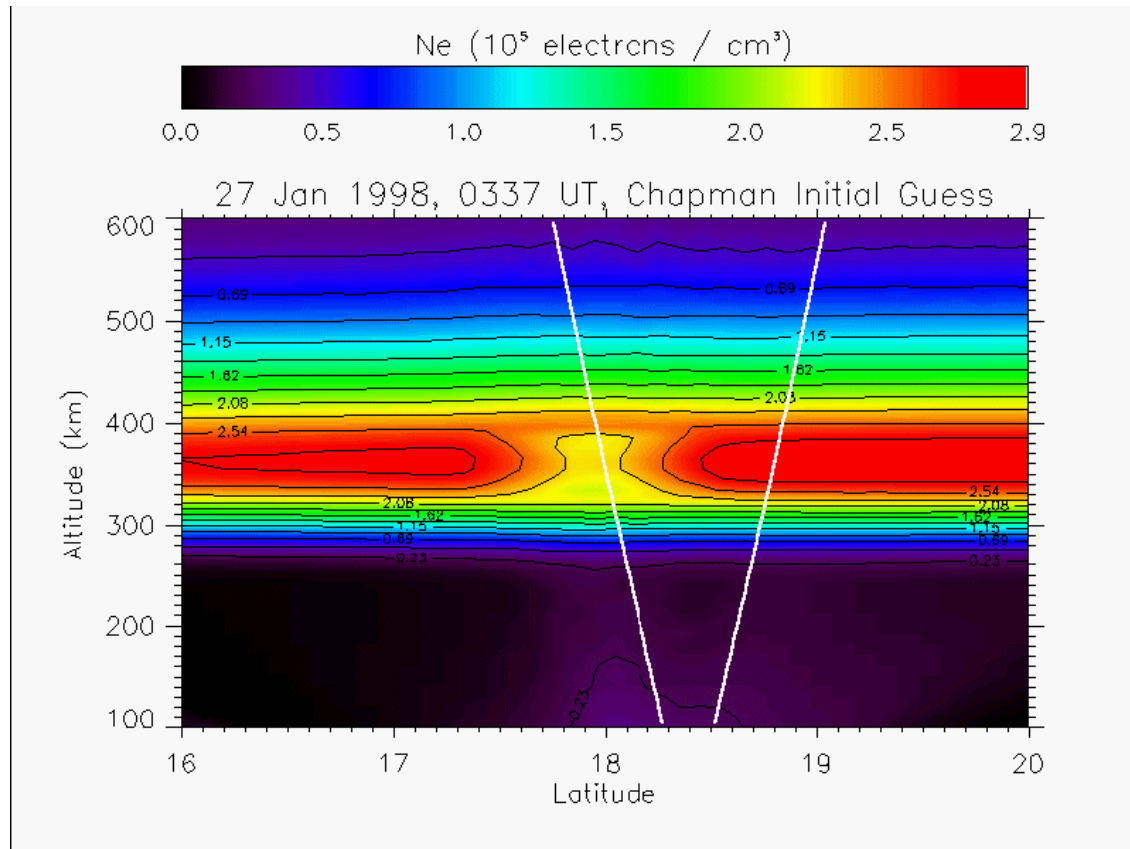Figure 15c: Eastern Chain Reconstruction, Chapman Initialization

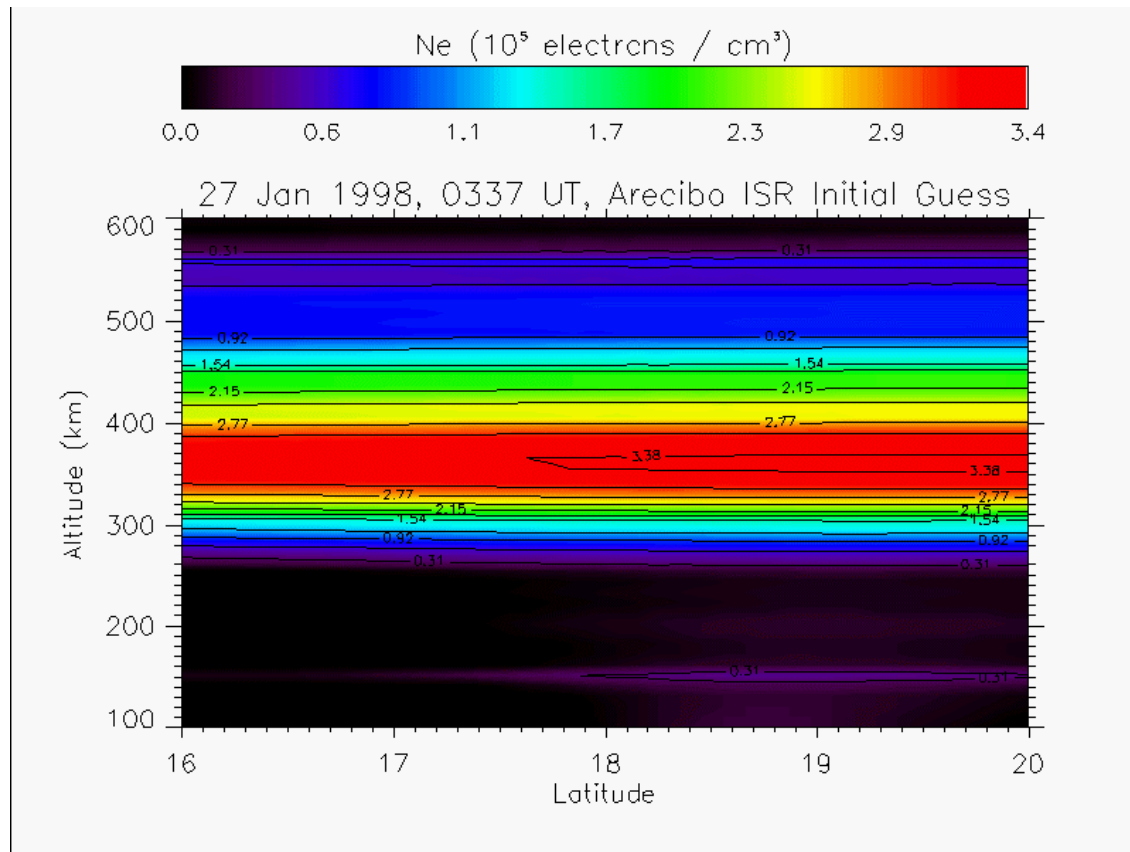Figure 16a: Western Chain Reconstruction, ISR Initialization

Figure 16b: Central Chain Reconstruction, ISR Initialization

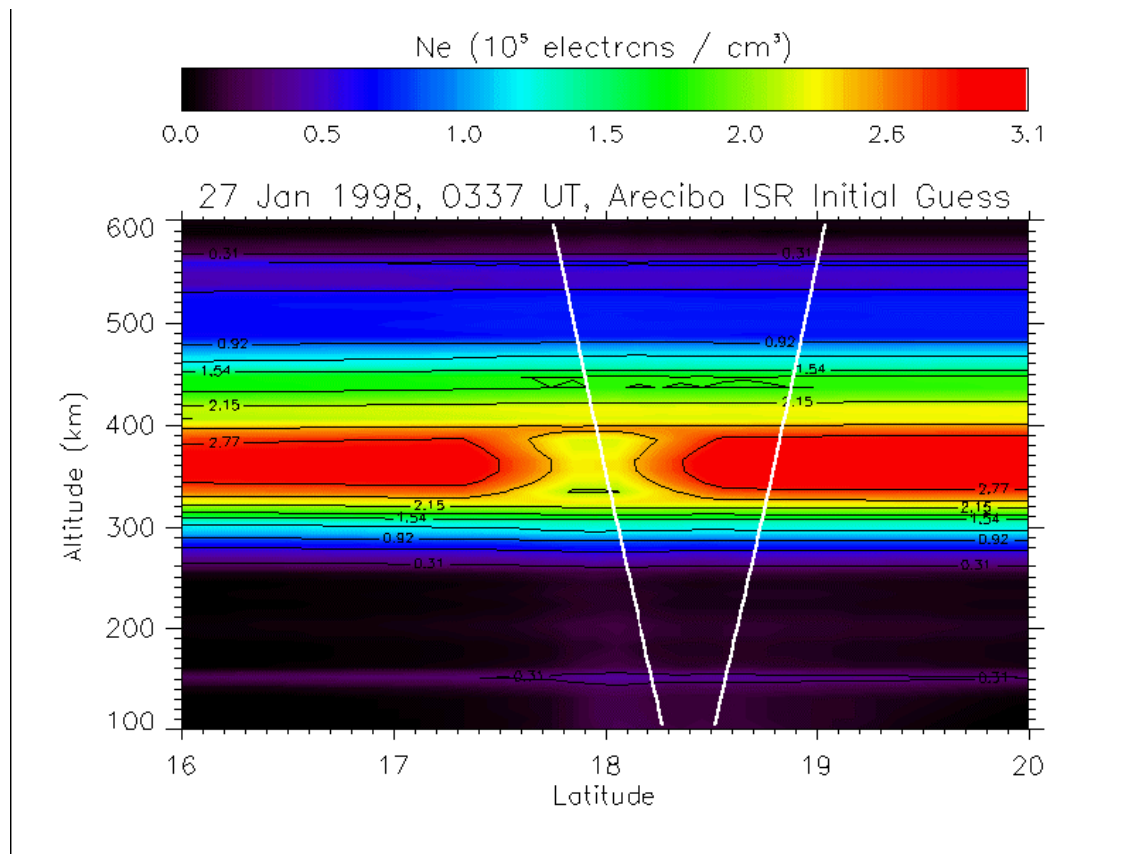Figure 16c: Eastern Chain Reconstruction, ISR Initialization

Figure 17: ISR Temperature Data and n_e Scaling Factor
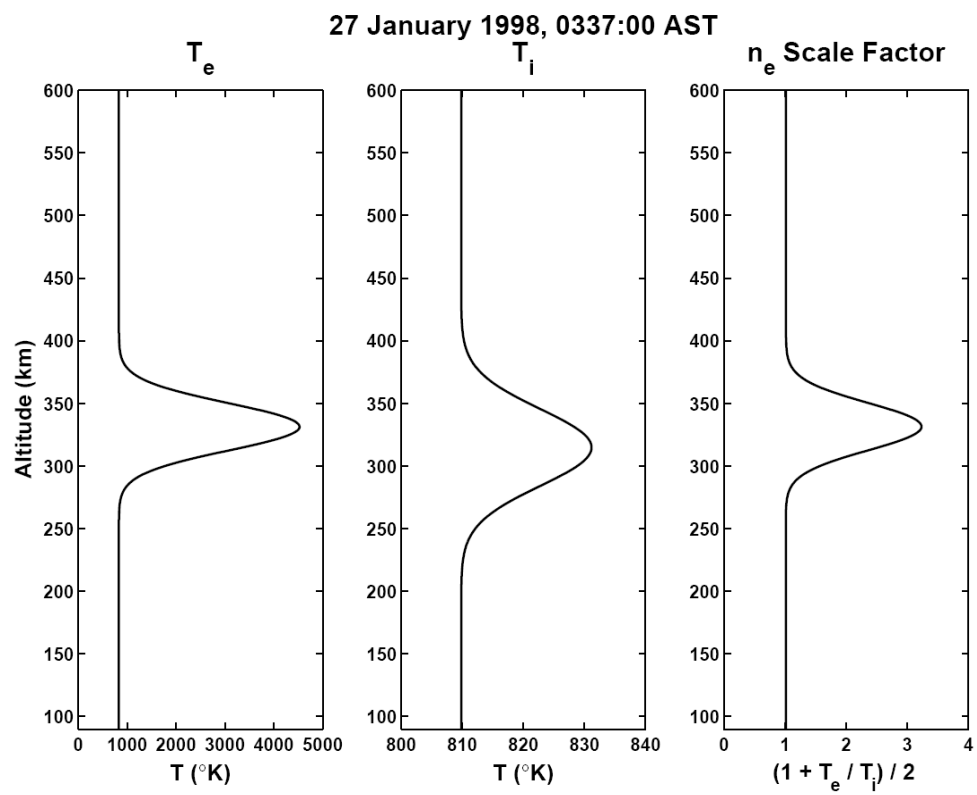
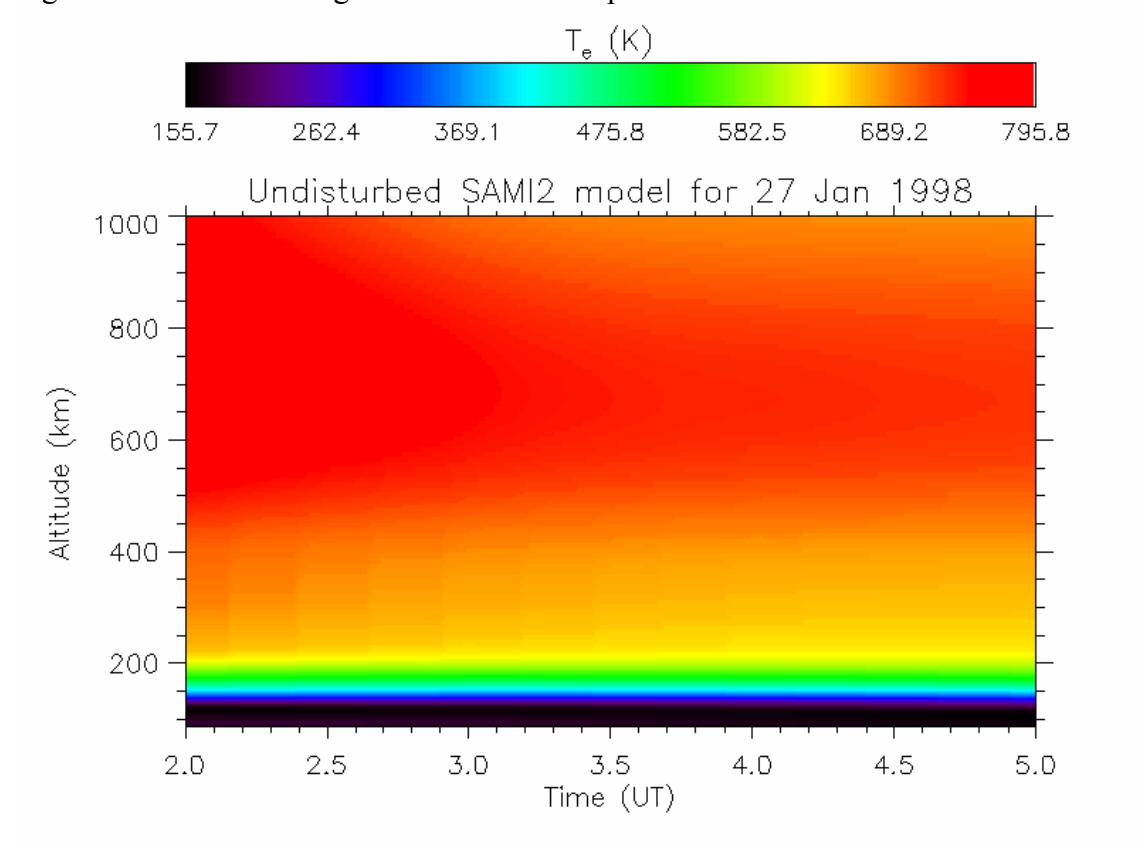Figure 18: SAMI2 Background Electron Temperature

Figure 19: SAMI2 Heated Electron Temperature
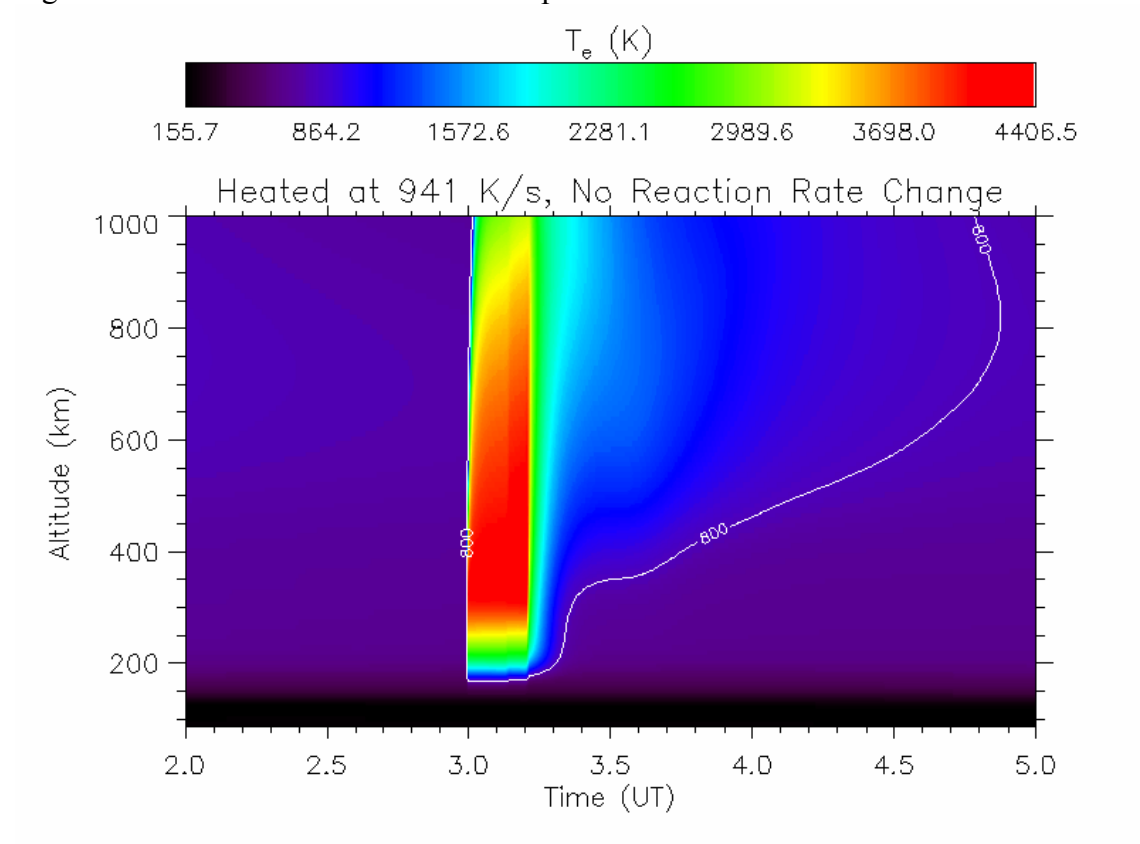
Figure 20: SAMI2 Change in Electron Temperature Due to Heating

Figure 21: SAMI2 Background Electron Density

Figure 22: SAMI2 Heated Electron Density
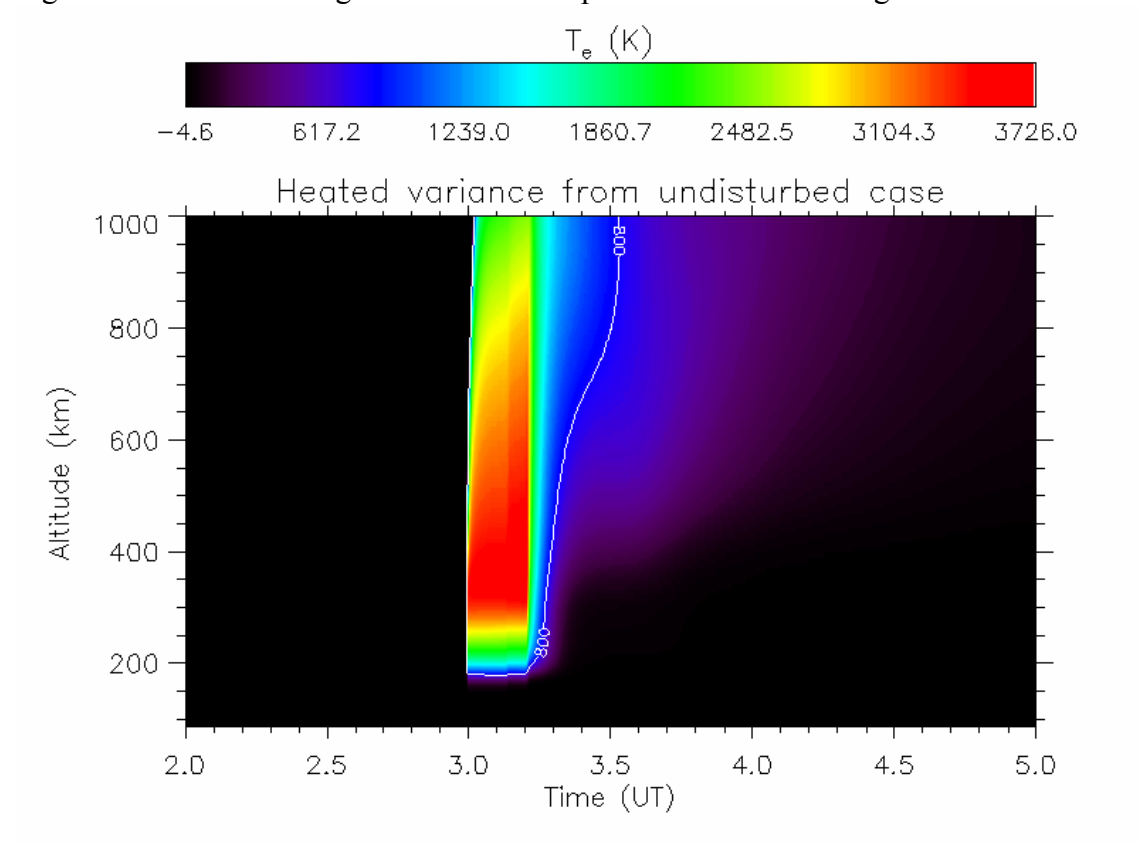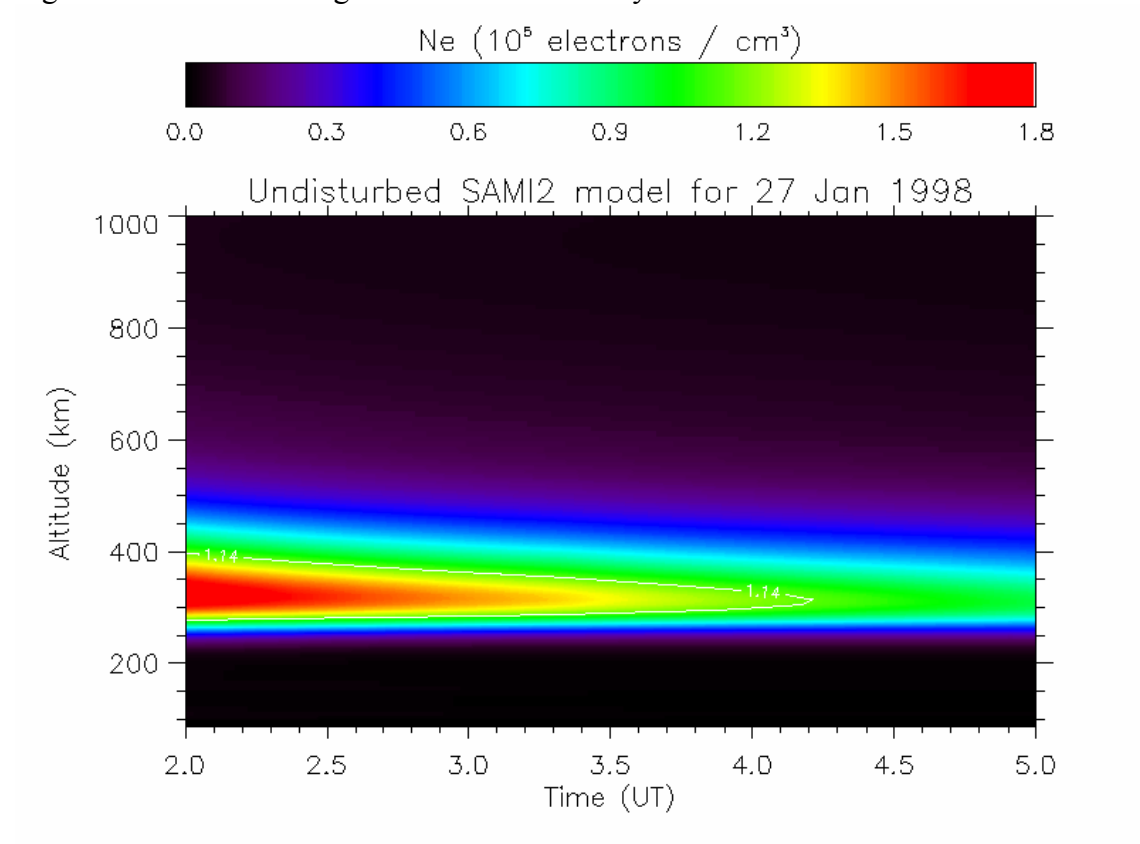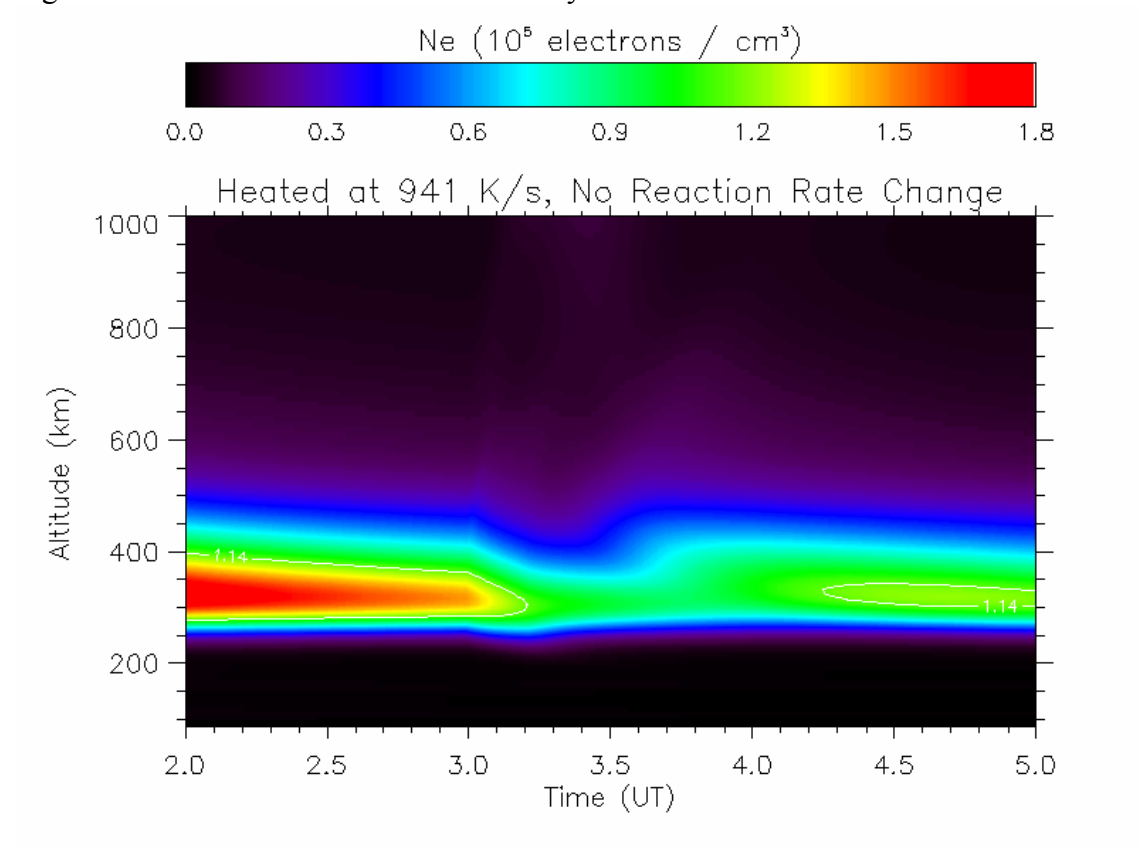
Figure 23: SAMI2 Change in Electron Density Due to Heating
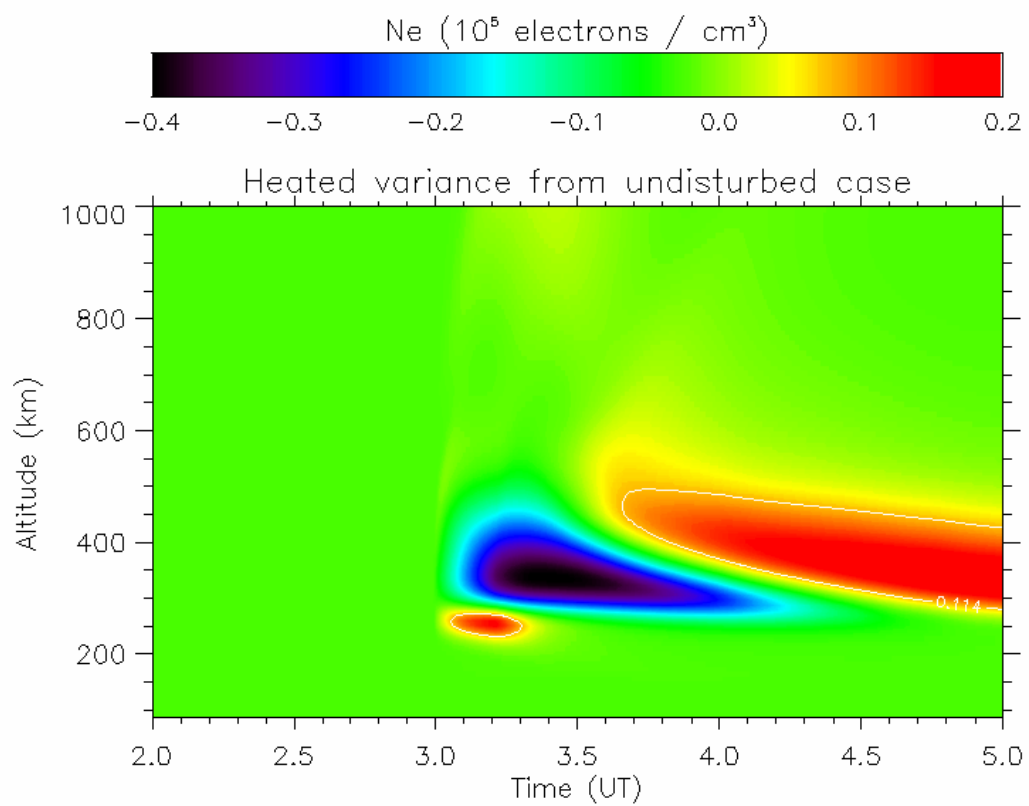

Ne (10⁵ electrons / cm³)

Figure 24: Change in Electron Density Due to Heating and Reaction Rate Effects

Figure 25: SAMI2 Final Modeling Result
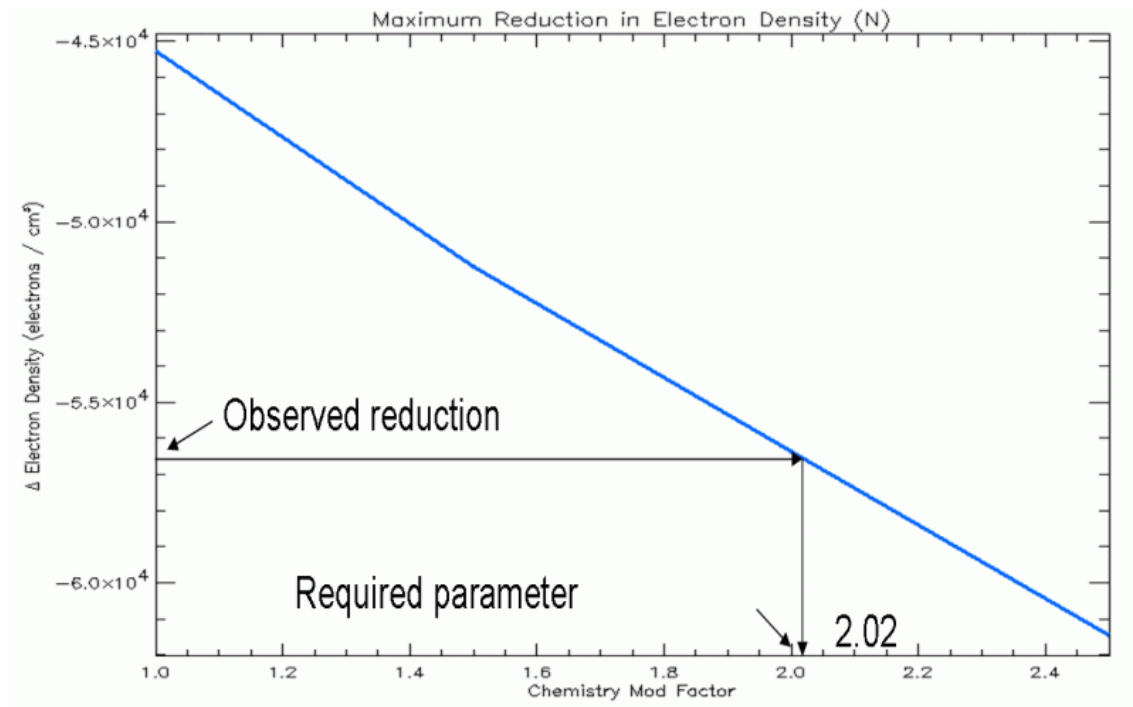

Δ Ne (10⁵ electrons / cm³)

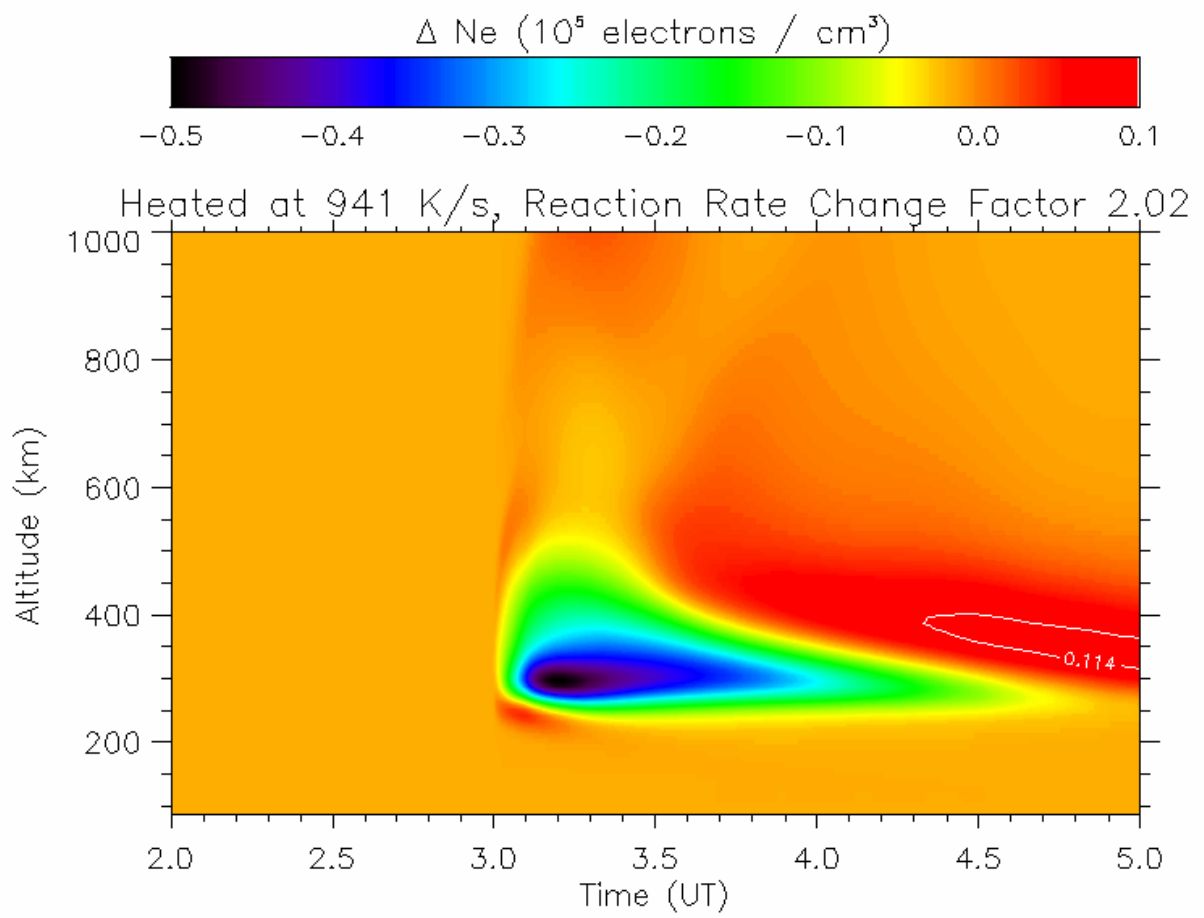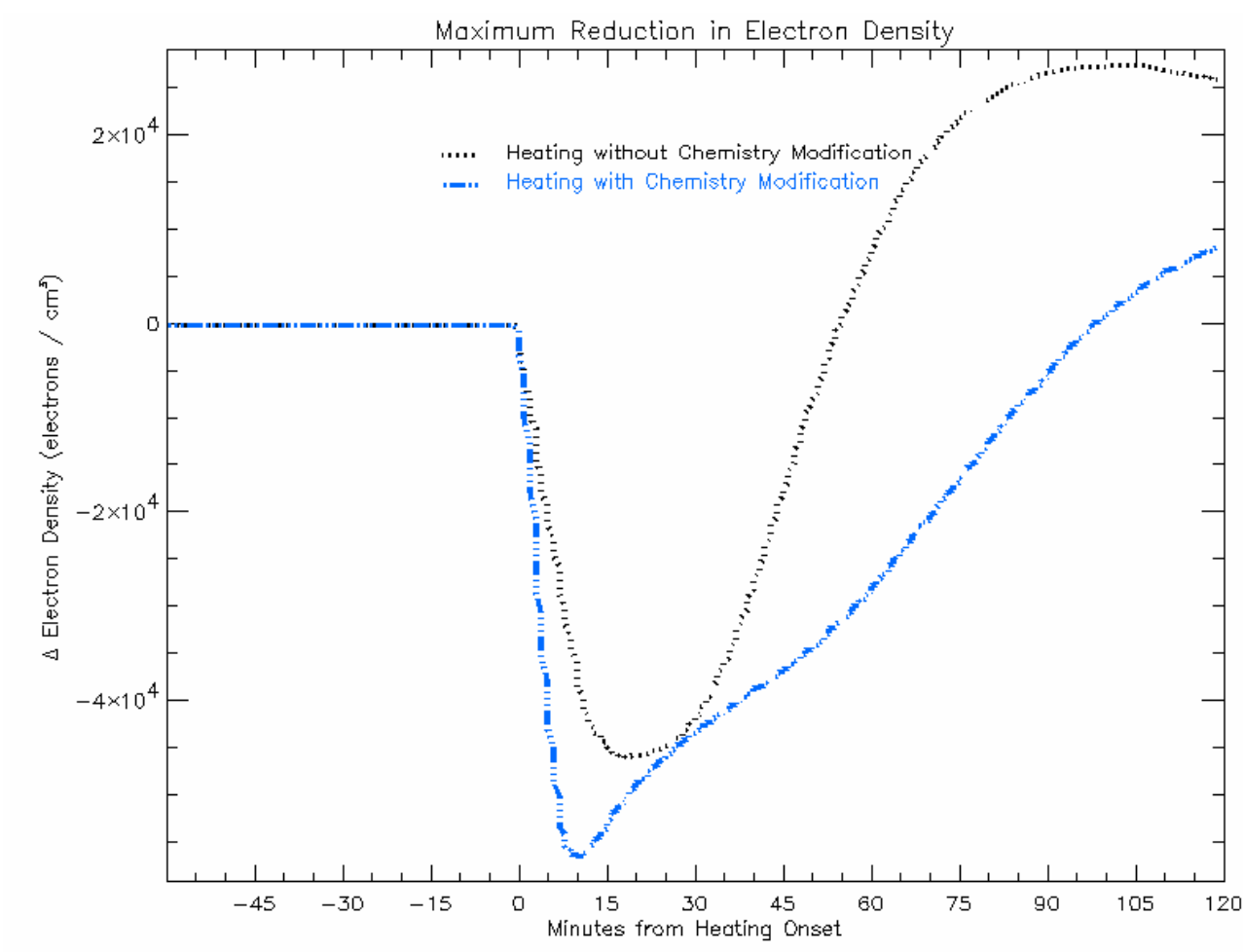Heated at 941 K/s, Reaction Rate Change Factor 2.02

Figure 26: Chemistry Effect Comparison

APPENDIX A: CIT Reconstruction Software

The Algebraic Reconstruction Technique (ART) based CIT code follows. It is written in the Interactive Data Language (IDL) developed by Research systems, Inc. IDL is based on the Fortran programming language, but has a number of features which make it an excellent tool for scientific research. In particular, operators and functions work on entire array without using loops, reducing programming time and making interactive data analysis more straightforward.

```
;+
;   ARTalpha1.PRO
;
;       Loads TEC data from specified directory,
;       Calculates the D matrix,
;       Initializes X matrix,
;       Solves Y=DX for X using the ART algorithm
;          uses regular grid
;       Final image is in units of 1e16 electrons per cubic meter
;     2-> receiver locations adjusted
;-

function loadtecdata, datadir=datadir,absol=absol,$
           minlat=minlat, maxlat=maxlat, $
           minrad=minrad, maxrad=maxrad
; loads all TEC data in specified directory,
;     determines which raypaths are inside the image space,
;   returns the tec and position data for each path,
;   the average Chapman parameters, and the number of paths Np
    files = findfile((datadir + '*.tec'),Count=numfiles)
    filesf = files
    for j=0,(numfiles-1) do begin
        datalength=strlen(files[j])
        filesf[j] = strmid(files[j],0,datalength-3) + 'f33'
    endfor
    if numfiles eq 0 then message,'No tec files in the specified
directory!'

    pcount = 0L
    nfiles = 0

    for j=0L,numfiles-1 do begin
        t=loadtec(filename=files[j])
        ;f=loadfit(filename=filesf[j])
        ;atec = atec + min(f.tecf)
        ;chap_p[j,*] = f.p
        ;hdr[j] = t.hdr
        pcount = pcount + n_elements(t.sat_lat)
    endfor
    tptecf = fltarr(pcount)  ;   fitted tec for path i
    tptecg = fltarr(pcount)  ;   fitted tec for path i w/geof
    tpglat = fltarr(pcount)  ;   ground int_box lat for path i
    tpslat = fltarr(pcount)  ;   sat int_box lat for path i
    tp4lng = fltarr(pcount)  ;   400km lng for path i
```

```
    tpgeof = fltarr(pcount)  ;   geometric factor for path i
    tpfile = 0*intarr(pcount)  - 1;   file num for path i
    Np      = 0L                     ;    path total
    Nps    = 0L                     ;    path subtotal
    lbound1 = intarr(numfiles)
    ubound1 = intarr(numfiles)
    for j=0L,numfiles-1 do begin
      Nps  = Np                     ;    initial path subtotal
        t=loadtec(filename=files[j])
        f=loadf33(filename=filesf[j])
        atec = (f.satec + f.catec + f.natec)/3.0
        elv = max(t.sat_elv)
        tcount = n_elements(t.sat_lat)
        for i = 0L,tcount-1 do begin
            ; determine where the path intercepts the image box:
            ;  and use 0.15 to correct for A98 receiver lat error:
            int_boxs = getlatlon((maxrad-6378.0) , $

      ;[((t.hdr[1]+0.15)/!RADEG),(t.hdr[2]/!RADEG),(t.hdr[3]-
6378.0)],$

      [((t.hdr[1])/!RADEG),(t.hdr[2]/!RADEG),(t.hdr[3]-6378.0)],$
                      (t.sat_elv[i]/!RADEG) , (t.sat_azm[i]/!RADEG)
)
            int_boxg = getlatlon((minrad-6378.0) , $

      ;[((t.hdr[1]+0.15)/!RADEG),(t.hdr[2]/!RADEG),(t.hdr[3]-
6378.0)],$

      [((t.hdr[1])/!RADEG),(t.hdr[2]/!RADEG),(t.hdr[3]-6378.0)],$
                      (t.sat_elv[i]/!RADEG) , (t.sat_azm[i]/!RADEG)
)
            if not((int_boxs[0]*!RADEG lt minlat) or $
                  (int_boxs[0]*!RADEG gt maxlat) or $
                  (int_boxg[0]*!RADEG lt minlat) or $
                  (int_boxg[0]*!RADEG gt maxlat) or $
                  ;(t.hdr[1]+0.15  lt minlat) or $
                  ;(t.hdr[1]+0.15  gt maxlat)) then begin
                  (t.hdr[1] lt minlat) or $
                  (t.hdr[1] gt maxlat)) then begin
                  tpglat[Np] = int_boxg[0]*!RADEG
                  tpslat[Np] = int_boxs[0]*!RADEG
                  if (absol) then begin
                        tptecf[Np] = 1e12*(t.tecs[i])
                        endif else begin
                        tptecf[Np] = 1e12*(t.tecs[i] + atec) ; TEC,
using fitted offset
                  endelse
                  tpgeof[Np] = cos( (90-(elv+abs(t.lng_400[i]-
t.hdr[2])))/!RADEG )
                  if (absol) then begin
                        tptecg[Np] = 1e12*(t.tecs[i] )*tpgeof[Np] ;
TEC w/geof
                        endif else begin
```

```
                              tptecg[Np] = 1e12*(t.tecs[i]+ min(f.tecf)
)*tpgeof[Np] ; TEC w/geof
                endelse
                              tp4lng[Np] = t.lng_400[i]
                              tpfile[Np] = j
                      Np = Np + 1

         endif
       endfor
       if (Nps ne NP) then begin
           nfiles = nfiles+1
           lbound1[j] = Nps   ; lower path bound for file j
           ubound1[j] = Np-1  ; upper path bound for file j
       endif
    endfor
    tpfile = tpfile[where(tpfile ge 0)]
    ps = fltarr(nfiles,3)
    pc = fltarr(nfiles,3)
    pn = fltarr(nfiles,3)

      slat = fltarr(nfiles)
      clat = fltarr(nfiles)
      nlat = fltarr(nfiles)

    hdr = fltarr(nfiles, 35)
    flist = tpfile[uniq(tpfile,sort(tpfile))]
    lbound = intarr(nfiles)
    ubound = intarr(nfiles)
      for j=0L,nfiles-1 do begin
           lbound[j] = lbound1[flist[j]]
           ubound[j] = ubound1[flist[j]]
           tpfile[lbound[j]:ubound[j]] = flist[j]
           t=loadtec(filename=files[flist[j]])
         f=loadf33(filename=filesf[flist[j]])
           ps[j,*] = f.ps
           pc[j,*] = f.pc
           pn[j,*] = f.pn
           slat[j] = f.slat
           clat[j] = f.clat
           nlat[j] = f.nlat
           hdr[j,*]    = t.hdr
      endfor
      pfile = tpfile[0:Np-1]  ;   file num for path i
    ptecf = tptecf[0:Np-1]  ;   fitted tec for path i
    ptecg = tptecg[0:Np-1]  ;   fitted tec for path i w/geof
    pglat = tpglat[0:Np-1]  ;   ground box_int lat for path i
    pslat = tpslat[0:Np-1]  ;   sat box_int lat for path i
      pgeof = tpgeof[0:Np-1]  ;   geometric factor
      p4lng = tp4lng[0:Np-1]  ;   lat_400 intersection for path i
      ;
      t = { hdr            : hdr, $
            lbound         : lbound,$
            ubound         : ubound,$
            ps               : ps, $
```

```
                 pc                : pc, $
                 pn                : pn, $
                 slat              : slat, $
                 clat                  : clat, $
                 nlat                    : nlat, $
                 ptecf             : ptecf, $
                 ptecg             : ptecg, $
                 pglat             : pglat, $
                 pslat             : pslat, $
                 pgeof             : pgeof, $
                 p4lng             : p4lng, $
                 nfiles            : nfiles, $
                 Np                : Np, $
                 pfile             : pfile $
                 }
         return, t
END

function calcpaths, lgrid,nbl,rgrid,nbr,pglat,pslat,Np,Nb,$
                   plotpaths=plotpaths, ith=ith,cith=cith
       if n_elements(plotpaths) eq 0 then plotpaths=0 ;else plotpaths =
1
       if n_elements(ith) eq 0 then ith = 5
       if n_elements(ith) eq 0 then ith = 2
       dsize = nbl+nbr
       ; cell index, path i, segment j:
       icell = lindgen(Np,dsize)
       icell = 0L*icell - 1L
       ; cell length, path i, segment j:
       dcell = findgen(Np,dsize)
       dcell = 0.0*dcell - 1.0
     dlgrid = 0.5*(max(lgrid) - min(lgrid))/(float(Nbl)-1)
     drgrid = 0.5*(max(rgrid) - min(rgrid))/(float(Nbr)-1)
     maxlgrid = lgrid + dlgrid
     minlgrid = lgrid - dlgrid
     maxrgrid = rgrid + drgrid
     minrgrid = rgrid - drgrid
     psrad=max(maxrgrid)
     pgrad=min(minrgrid)
       xg = pgrad*cos(pglat/!RADEG)
       yg = pgrad*sin(pglat/!RADEG)
       xs = psrad*cos(pslat/!RADEG)
       ys = psrad*sin(pslat/!RADEG)
       m  = (ys-yg)/(xs-xg)
     ib = yg - m*xg
     ; find rho and theta for polar line equation:
     ; rho = rad*cos(lat-theta)
     ; rad = rho/cos(lat-theta)
     ; lat = acos(rho/rad) + theta
     rho = ib/sqrt(m*m+1)
     theta = !RADEG*atan(-1,m)
     test= where(rho lt 0,count)
     if count ne 0 then begin
         theta[test]=theta[test]+180
```

```
          rho[test]=abs(rho[test])
      endif
      test= where(theta lt 0,count)
      if count ne 0 then begin
          theta[test]=theta[test]+360
      endif
      rint=indgen(Nbr)
      lint=indgen(Nbl)
      rv = dindgen(Nbr+1)
      lv = dindgen(Nbl+1)
      rv[0:(Nbr-1)] = double(minrgrid[Nbl*rint])  ;grid radius values
      rv[Nbr] = double(max(maxrgrid))
      lv[0:(Nbl-1)] = double(minlgrid[lint])      ;grid latitude values
      lv[Nbl] = double(max(maxlgrid))
      if plotpaths then begin
        set_plot,'PS'

      device,filename='c:\research\working\pathplot.ps',/inches,xsize=
10,ysize=7.5,/landscape,xoffset=.5,yoffset=10.5,/color
        loadct,0
        ;window,2,xsize=900, ysize=700
        plot,pglat,pglat,/nodata,$
             /ystyle,yrange=[min(minrgrid)-6378,max(maxrgrid)-
6378],yticks=1,$
             /xstyle,xrange=[min(minlgrid),max(maxlgrid)],xticks=1,$
             title  = 'Paths through the image plane',$
             xtitle =  'Latitude',$
             ytitle =  'Altitude (km)'
      endif
      for i = 0,(Np-1) do begin
        ; latitude where path i intercepts each gridded radius:
        if (pslat[i]-pglat[i] gt 0) then begin
             lat_rgrid = double(theta[i] + !RADEG*acos(rho[i]/rv))
             endif else begin
                   lat_rgrid = double(theta[i] -
!RADEG*acos(rho[i]/rv))
        endelse
        test = where(lat_rgrid gt 90.0,count)
        if count gt 0 then lat_rgrid[test] = lat_rgrid[test] - 180.0
        test = where(lat_rgrid lt -90.0,count)
        if count gt 0 then lat_rgrid[test] = lat_rgrid[test] + 180.0
        ; radii for those latitudes:
             rad_rgrid = rv
             ; radii where path i intercepts each gridded latitude:
        rad_lgrid = double(abs(rho[i]/cos((lv - theta[i])/!RADEG)))
             ; latitudes for those radii:
        if (pslat[i]-pglat[i] gt 0) then begin
             lat_lgrid = double(theta[i] +
!RADEG*acos(rho[i]/rad_lgrid))
             endif else begin
                   lat_lgrid = double(theta[i] -
!RADEG*acos(rho[i]/rad_lgrid))
        endelse
        test = where(lat_lgrid gt 90.0,count)
```

```
        if count gt 0 then lat_lgrid[test] = lat_lgrid[test] - 180.0
        test = where(lat_lgrid lt -90.0,count)
        if count gt 0 then lat_lgrid[test] = lat_lgrid[test] + 180.0
        ; now reduce them to be inside the image box
        test = where( (lat_rgrid ge (min(minlgrid))) and (lat_rgrid le
(max(maxlgrid))) and $
                                (rad_rgrid ge (min(minrgrid))) and
(rad_rgrid le (max(maxrgrid))),count)
        ;if (count ne 0) then begin
                lat_rgrid=lat_rgrid[test]
            rad_rgrid=rad_rgrid[test]
        ;endif
            test = where( (lat_lgrid ge (min(minlgrid))) and
(lat_lgrid le (max(maxlgrid))) and $
                                (rad_lgrid ge (min(minrgrid))) and
(rad_lgrid le (max(maxrgrid))),count)
            vert_flag=0
        if (count ne 0) then begin
                lat_lgrid=lat_lgrid[test]
            rad_lgrid=rad_lgrid[test]
        endif else begin
            vert_flag = 1
            lat_lgrid = 100
            rad_lgrid = 100
        endelse
            ; collect cell intersections into sequential pairs:
            if (vert_flag eq 1) then begin
                lat_pgrid = double(lat_rgrid)
                rad_pgrid = double(rad_rgrid)
            endif else begin
                lat_pgrid = double([lat_rgrid,lat_lgrid])
                rad_pgrid = double([rad_rgrid,rad_lgrid])
            endelse ; end vert_flag condition
            sindex = sort(rad_pgrid)
            lat_pgrid = lat_pgrid[sindex]
            rad_pgrid = rad_pgrid[sindex]
        ; determine cells and D values for each sequential pair
            ; d-value = sqrt[ ro^2 + r1^2 - 2r1r2cos(phi1-phi2)]
            for j = 0, (n_elements(lat_pgrid)-2) do begin
                lat_seg = 0.5*(lat_pgrid[j] + lat_pgrid[j+1])
                rad_seg = 0.5*(rad_pgrid[j] + rad_pgrid[j+1])
                ind = where(  (lat_seg ge minlgrid) AND $
                                        (lat_seg le maxlgrid) AND $
                                        (rad_seg ge minrgrid) AND $
                                        (rad_seg le maxrgrid))
                sind = size(ind)
                if sind[0] ne 1 then print, 'ERROR: multi-
intersection: dim =',sind[0]
                icell[i,j] = ind[0]
                dcell[i,j] = sqrt( rad_pgrid[j]*rad_pgrid[j] +
rad_pgrid[j+1]*rad_pgrid[j+1] - 2*rad_pgrid[j]*rad_pgrid[j+1]*cos(
(lat_pgrid[j] - lat_pgrid[j+1]) / !RADEG) )
            endfor; icell loop
            ;print,i,vert_flag
```

```
            if plotpaths and (i mod ith eq 0) then
oplot,lat_pgrid,rad_pgrid-6378
            if ( (i+1) mod 100 eq 0) then print,'Finished path ',i+1,'
of ', Np
      endfor ; path loop
      if plotpaths then begin
            ; draw lat grid
            for k = 0, nbl-1,cith do $
                  plots,[minlgrid[k],minlgrid[k]],[min(minrgrid)-
6378,max(maxrgrid)-6378], color= 200
            plots,[max(maxlgrid),max(maxlgrid)],[min(minrgrid)-
6378,max(maxrgrid)-6378], color= 200
            for k = 0, nbr-1,cith do $

      plots,[min(minlgrid),max(maxlgrid)],[minrgrid[k*nbl]-
6378,minrgrid[k*nbl]-6378], color= 200
            plots,[min(minlgrid),max(maxlgrid)],[max(maxrgrid)-
6378,max(maxrgrid)-6378], color= 200
            ;win2gif,filename='c:\research\working\pathplot.gif'
            device,/close_file
            set_plot,'WIN'
      endif
      print,'done'
      dcell = dcell * 1e5            ; convert from km to cm
      D =   {     icell         : icell, $
                  dcell         : dcell}
      return, D
END

function chapinit,lats,rgrid,ps,pc,pn,slat,clat,nlat,nbl,nbr
      chap = reform(rgrid,nbl,nbr)
      cz = reform(chap[0,*])
      asize = n_elements(slat)
      pz = findgen(3*asize)
      pne = findgen(3*asize)
      ph = findgen(3*asize)
      plats = findgen(3*asize)

      pz[0:asize-1] = ps[*,0]
      pz[asize:2*asize-1] = pc[*,0]
      pz[2*asize:3*asize-1] = pn[*,0]

      pne[0:asize-1] = ps[*,1]
      pne[asize:2*asize-1] = pc[*,1]
      pne[2*asize:3*asize-1] = pn[*,1]

      ph[0:asize-1] = ps[*,2]
      ph[asize:2*asize-1] = pc[*,2]
      ph[2*asize:3*asize-1] = pn[*,2]

      plats[0:asize-1] = slat[*,0]
      plats[asize:2*asize-1] = clat[*,0]
      plats[2*asize:3*asize-1] = nlat[*,0]
```

```
      sindex = sort(plats)
      pz = pz[sindex]
      pne = pne[sindex]
      ph = ph[sindex]
      plats = plats[sindex]

      pzi = spline(plats,pz,lats,.01)
      pni = spline(plats,pne,lats,.01)
      phi = spline(plats,ph,lats,.01)
      pzi = smooth(pzi,fix(nbl/50 + 3))
      pni = smooth(pni,fix(nbl/50 + 3))
      phi = smooth(phi,fix(nbl/50 + 3))

      ;pzi = interpol(pz,plats,lats)
      ;pni = interpol(pne,plats,lats)
      ;phi = interpol(ph,plats,lats)

      for i=0,n_elements(lats)-1 do chap(i,*) =
chap_3(pzi[i],pni[i],phi[i],cz)
      chap = smooth(chap,fix(nbl/50 + 3))
      chap = reform(chap,nbl*nbr)
      return,chap
END

function get_dmap,D,nbl,nbr
      dmap = 0.0*findgen(nbl*nbr)
      s=size(d.icell)
      for i = 0,(s[1]-1) do begin
            for j=0,(s[2]-1) do begin
                  if d.icell[i,j] ge 0 then $
                        dmap[d.icell[i,j]] = dmap[d.icell[i,j]] +
d.dcell[i,j]
            endfor
      endfor
    dmap = reform(temporary(dmap),nbl,nbr)
    return,dmap
END

PRO artalpha1, datadir=datadir, savefile=savefile,Dmatrix=Dmatrix,$
        Xinit=xinit, Xfinal=Xfinal,
Nbl=Nbl,Nbr=Nbr,noupdate=noupdate,$

ptecf=ptecf,dchimin=dchimin,chimin=chimin,iterloops=iterloops,$
        minlat=minlat,maxlat=maxlat,minrad=minrad,maxrad=maxrad,$
        lgrid=lgrid,rgrid=rgrid,plotpaths=plotpaths, ith=ith,
absol=absol,cith=cith,$
        initmatch=initmatch,initlambda=initlambda,nomchap=nomchap
    device,decomposed=0
    cleanwin
    if n_elements(absol) eq 0 then absol = 0
    if n_elements(noupdate) eq 0 then noupdate = 0
    if n_elements(initmatch) eq 0 then initmatch = 0
    if n_elements(initlambda) eq 0 then initlambda = .01
    if n_elements(chimin) eq 0 then chimin = 5e-3
```

```
    if n_elements(dchimin) eq 0 then dchimin = 1e-6
    if n_elements(iterloops) eq 0 then iterloops = -1L
    if n_elements(nomchap) eq 0 then nomchap = 0
    itime=systime()
    print,'Starting on ',itime
    savelength = strlen(datadir)
    if n_elements(savefile) eq 0 then savefile = $
      strmid(datadir,0,(savelength - 1)) + '.art'
    savelength = strlen(savefile)
    tecfile = strmid(savefile,0,(savelength - 4)) + '_tec.gif'
    giffile = strmid(savefile,0,(savelength - 4)) + '_tomo.gif'
    dmapfile = strmid(savefile,0,(savelength - 4)) + '_dmap.gif'
    xinitfile = strmid(savefile,0,(savelength - 4)) + '_init.gif'
; load satellite and receiver position, and fitted tec data
    if n_elements(datadir) eq 0 then
file=dialog_pickfile(get_path=datadir,$
        title='Select a file in the directory you wish to process',$
        filter='*.tec',path='d:\working\')
    print,'Loading TEC data...'
      t = loadtecdata(datadir=datadir,absol=absol,$
            minlat=minlat,maxlat=maxlat,$
            maxrad=maxrad, minrad=minrad)
      set_plot,'WIN'
    !p.multi=0
    device,decomposed=0
    window,2,xsize=700,ysize=500
    plottec,t.pglat,tcec1,st=sub,/ystyle,$
      yrange=[min(t.ptecg)/(1e12)-
1.0,(max(t.ptecg)/1e12)+1.0],/nodata,$
      xt='Image Intercept Latitude',pt='Absolute TEC',$
      BACKGROUND = 255, COLOR = 0, minlat=minlat,maxlat=maxlat
      for j = 0, t.nfiles-1 do
oplot,t.pslat[t.lbound[j]:t.ubound[j]],$

      t.ptecg[t.lbound[j]:t.ubound[j]]/1e12,linestyle = j+1
      win2gif, filename=tecfile

; create reconstruction grid
    print,'Initializing reconstruction configuration...'
    ; # of pixels on latitude 'side' of reconstruction image:
    if n_elements(Nbl) eq 0 then Nbl = 20
    ; # of pixels on radius 'side' of reconstruction image:
    if n_elements(Nbr) eq 0 then Nbr = 20
    ; # of pixels (total):
    Nb = Nbl*Nbr
    if ( (n_elements(rgrid) eq 0) or (n_elements(lgrid) eq 0)) then
begin
        if n_elements(minlat) eq 0 then minlat = min(pslat)
        if n_elements(maxlat) eq 0 then maxlat = max(pslat)
        if n_elements(minrad) eq 0 then minrad = 6378.0 + 100.0
        if n_elements(maxrad) eq 0 then maxrad = 6378.0 + 600.0
        dlgrid = 0.5*(maxlat - minlat) / float(Nbl) ; 0.5 lat grid
spacing
```

```
        drgrid = 0.5*(maxrad - minrad) / float(Nbr) ; 0.5 rad grid
spacing
        ; lat coords of center of the box around each pixel:
        lgrid = fltarr(Nbl*Nbr)
        ; rad coords of center of the box around each pixel:
        rgrid = lgrid
        bi = indgen(Nbl*nbr)
        bl = (bi mod Nbl)
        lgrid[*] = 2*bl*dlgrid + dlgrid + minlat
        br = floor(bi/Nbl)
        rgrid[*] = 2*br*drgrid + drgrid + minrad
        undefine, bi
        undefine, bl
        undefine, br
    endif else begin
        minlat=min(lgrid)
        maxlat=max(lgrid)
        minrad=min(rgrid)
        maxrad=max(rgrid)
    endelse
    dtstamp = ss2hhmm(t.hdr[0,8]) + ' on DOY ' + $
      strcompress(string(fix(t.hdr[0,7])),/remove_all) + $
        ' of ' + strcompress(string(fix(t.hdr[0,6])),/remove_all)
; initialize reconstruction configuration
    stime=systime()
    print,'Calculating Dmatrix of ',t.Np,' paths through pixel grid
on: ',stime
    if n_elements(Dmatrix) ne 0 then s=size(Dmatrix.dcell) else
s=[0,0,0]
    dsize = nbl+nbr
    if ((s[1] ne t.Np) or (s[2] ne (dsize))) then begin
        print,'...performing calculations'
        D =
calcpaths(lgrid,Nbl,rgrid,Nbr,t.pglat,t.pslat,t.Np,Nb,plotpaths=plotpa
ths,ith=ith,cith=cith)
    endif else begin
            print,'...Using loaded Dmatrix array'
            D = Dmatrix
    endelse
    stime=systime()
    print,'Finished Dmatrix calculation on              : ',stime
    dmap = get_dmap(D,nbl,nbr)
    loadct,39
    window,0,xsize=795,ysize=543,title='Dmap',xpos=0,ypos=0
    erase,255
      plotrecon,dmap,rgrid,nbr,lgrid,nbl,ptitle='Path Density
Map',btitle='Total path length per cell (km)'
    ;xyouts,.3,.82,dtstamp,/normal,color=0,charsize=1.5
    win2gif,filename=dmapfile
    window,0,xsize=395,ysize=540,title='Dmap',xpos=0,ypos=0
    erase,0
    plotrecon,dmap,rgrid,nbr,lgrid,nbl,ptitle='Path Density
Map',btitle='Total path length per cell (km)'
    ;xyouts,.3,.82,dtstamp,/normal,color=255,charsize=1.5
```

```
  ; initialize X array
    ;pmean = fltarr(5)
    ;for j=0, 2 do begin
    ;    pmean[j] = total(t.chap_p[*,j]) / t.nfiles
    ;endfor
    if n_elements(xinit) eq 0 then begin
        print,'Generating initial Chapman guess...'
        Xinit=fltarr(Nb)
        if (nomchap) then begin
            Xinit = chap_3(6700.0, 1.5e6, 50,rgrid) ; use 'nominal'
chapman
        endif else begin ; use interpolated Chapman
            lats = lgrid[0:nbl-1]
            Xinit=chapinit(lats,rgrid, t.ps, t.pc, t.pn, t.slat,
t.clat, t.nlat, nbl,nbr)
        endelse
    endif else print,'Using loaded initial guess...'
      Xinit = Xinit * (dmap gt 0)
    ; determine absolute TEC of the image and match image to TEC data
    ; necessary at this time due to improperly calibrated ISR data
(4/20/01)
      ximage=reform(xinit,nbl,nbr)
      atec_xinit  = total(drgrid*2*1e5*ximage[floor(nbl/2),*])
      xmod  = min(t.ptecg)/atec_xinit
      print,'Atec: ',min(t.ptecg),'    Xinit Atec: ',atec_xinit,'
Xmod: ', xmod
      if (absol) then xmod=1.0
      xinit = xinit*xmod
      minX  = xinit * 0.0

    ;maxX  = chap_3(6728.0, 3.2e6, 40,rgrid)
    ;rcheck= where(rgrid lt 6728)
    ;gc = 3.2e6*exp(-.5*(rgrid-6728.0)^2/1.1e4)
    ;maxX[rcheck] = gc[rcheck]
    ;undefine,gc

    maxx = 5e6*exp(-.5*(rgrid-6728.0)^2/ 4e4  ) - 2.2e6 ; Gaussian
Maxx

    window,1,xsize=800,ysize=600,title='Initial Guess',xpos=0,ypos=0
    erase,255
    plotrecon,xinit,rgrid,nbr,lgrid,nbl,ptitle='Initial Guess'
    win2gif,filename=xinitfile
    window,1,xsize=395,ysize=540,title='Initial Guess',xpos=0,ypos=0
    erase,0
    plotrecon,xinit,rgrid,nbr,lgrid,nbl,ptitle='Initial Guess'
; begin iteration of ART
    print,'Commencing iteration...'
    X0 = Xinit
    X1 = X0
    chi0=total(t.ptecg*t.ptecg)
    loop = 1
    oldstatusline = ' '
    window,2,xsize=795,ysize=543,$
```

```
      title='Initial Reconstruction',xpos=0,ypos=0
    ximage=reform(x0,nbl,nbr)
    imagebar,ximage,xrange=[minlat,maxlat],$
      yrange=[minrad-6378.0,maxrad-6378.0],$
      xtitle='Latitude',ytitle='Altitude (km)'
    xyouts,.3,.82,dtstamp,/normal,color=255,charsize=1.5
    DL = findgen(t.Np)
    for i=0,(t.Np-1) do begin
      test = where(d.icell[i,*] ne -1)
      DL[i] = total(d.dcell[i,test])
    endfor
    D2 = DL*DL
    chi = t.ptecg
    chitest = 1.0
    s=size(d.icell)
    tval = 0.0
    lambda = 1
    image_tec = findgen(s[1])
    k=[[.1,.5,.1],[.5,24,.5],[.1,.5,.1]]

    repeat begin
        dchi = chitest
        X0 = X1
        err_tec = x1*0.0
      err_init = x1*0.0
        for i = 0,(s[1]-1) do begin ; sum over paths
                  test = where(d.icell[i,*] ne -1) ; select valid
segments
                  resid = total(d.dcell[i,test]*X1[d.icell[i,test]])
                  image_tec[i] = resid
                  art1 = (t.ptecg[i] - resid) / D2[i]
                  err_tec[d.icell[i,test]]  = err_tec[d.icell[i,test]]
+ lambda * art1 * d.dcell[i,test]
            endfor
            if (initmatch) then err_init = (initlambda*exp(-loop/30.0) +
.01)*(xinit-x1)
            X1 = X1 + err_tec + err_init
            if total(X1 lt minX) then begin
              Xi = long(where(X1 lt minX))
              X1[Xi] = minX[Xi]
        endif
        if total(X1 gt maxX) then begin
            Xi = long(where(X1 gt maxX))
            X1[Xi] = maxX[Xi]
        endif
; TEMPORARY!!!!
;REMOVE AFTER TESTING!!!
        x1= reform(x1,nbl,nbr)
        x1= convol(x1,k,total(k),/EDGE_TRUNCATE)
            x1= reform(x1,nbl*nbr)
;END TEST SECTION

        for i = 0,(s[1]-1) do begin ; sum over paths
```

```
                        test = where(d.icell[i,*] gt 0) ; select valid
segments
                    chi[i] = t.ptecg[i] -
total(d.dcell[i,test]*X0[d.icell[i,test]])
                endfor
                chitest = (total(chi*chi))/chi0
            dchi = abs(dchi-chitest)
            loop = loop+1L
            if (not noupdate) then begin
                    statusline = 'Iter: ' + $
                        strcompress(string(loop),/remove_all) + $
                        '  Chi: ' + $
strcompress(string(chitest,format='(E9.2)'),/remove_all) + $
                        ' dChi: ' + $
strcompress(string(dchi,format='(E9.2)'),/remove_all) + $
                        '  Max: ' + $
strcompress(string(max(X1),format='(E9.2)'),/remove_all) + $
                        ' Mean: ' + $
strcompress(string(total(X1)/n_elements(X1),format='(E9.2)'),/remove_a
ll)
                    print,statusline
                    ximage=reform(x1,nbl,nbr)
                    ;xmin = min(x1)
                    ;xmax = max(x1)
                    imagebar,ximage,xrange=[minlat,maxlat],$
                            yrange=[minrad-6378.0,maxrad-6378.0],$
                        xtitle='Latitude',ytitle='Altitude
(km)';,cmin=xmin,cmax=xmax
                    xyouts,.2,.77,oldstatusline,/normal,color=0,charsize=1.2
                    xyouts,.2,.77,statusline,/normal,color=255,charsize=1.2
                    oldstatusline=statusline
                endif
            X0 = X1
            ktest = GET_KBRD(0)
        endrep until ((dchi lt dchimin) or (loop eq iterloops) or $
                        ( chitest lt chimin) or ( ktest eq 'q'))
        statusline = dtstamp + ' ' + ' Iter: ' +
strcompress(string(loop),/remove_all)
        Xfinal=temporary(X1)
        window,3,xsize=800,ysize=600,title='Final
Reconstruction',xpos=0,ypos=0
        erase,0
        plotrecon,xfinal,rgrid,nbr,lgrid,nbl,ptitle='Final Reconstruction'
        win2gif,filename=giffile
        wshow,1
        window,3,xsize=800,ysize=600,title='Final
Reconstruction',xpos=0,ypos=0
        erase,0
        plotrecon,xfinal,rgrid,nbr,lgrid,nbl,ptitle='Final Reconstruction'
        t.Np = long(t.Np)
```

```
Nbl = long(Nbl)
Nbr = long(Nbr)
if n_elements(savefile) eq 0 then savefile =
'c:\research\working\recon.art'
openw, lun, savefile ,/Get_Lun
writeU, lun, t.Np
writeU, lun, Nbl
writeU, lun, Nbr
writeU, lun, D
writeU, lun, Xinit
writeU, lun, minX
writeU, lun, maxX
writeU, lun, Xfinal
writeU, lun, lgrid
writeU, lun, rgrid
writeU, lun, t.ptecf
writeU, lun, t.pgeof
free_lun,lun
print,'Started on  : ',itime
ftime=systime()
print,'Finished on : ',ftime

END
```